

## Masterarbeit

# EVALUATION OF THE MULTIPOLAR VENANT SOURCE MODELING APPROACH IN EEG SOURCE ANALYSIS

Fachbereich Mathematik und Informatik  
Westfälische Wilhelms Universität Münster

vorgelegt von: Carlotta Barkhau  
Matrikelnummer: 428918  
Erstgutachter: Prof. Dr. Carsten Wolters  
Zweitgutachter: Prof. Dr. Christian Engwer  
Abgabedatum: 14. Juni 2021

# Contents

<b>1</b>	<b>Introduction</b>	<b>1</b>
<b>2</b>	<b>The EEG Forward Problem</b>	<b>3</b>
2.1	Physiological Basics . . . . .	3
2.2	Mathematical Modeling . . . . .	5
2.3	Finite Element Method . . . . .	7
<b>3</b>	<b>Principle of Saint Venant</b>	<b>11</b>
3.1	Monopole Distribution . . . . .	11
3.2	Multipolar Venant Approach . . . . .	13
3.3	Computational Algorithm . . . . .	16
3.4	Error Estimation . . . . .	18
3.5	Monopolar Venant Approach . . . . .	19
<b>4</b>	<b>Quadrupolar Moments</b>	<b>21</b>
<b>5</b>	<b>Numerical Experiments</b>	<b>25</b>
5.1	Multi-layer Sphere Setups for Evaluation Studies . . . . .	25
5.2	The Software DUNEuro . . . . .	28
5.3	Venants Condition for the Multipolar Venant Approach . . . . .	31
5.4	Comparison of Multipolar and Monopolar Venant Approaches . . . . .	35
5.5	Approximation of Extended Sources . . . . .	39
<b>6</b>	<b>Conclusion</b>	<b>57</b>

## List of Figures

2.1	Human Brain [HÄ+93]	3
2.2	Illustration of a Neuron [BA+18]	4
3.1	Monopole Locations [KR19]	11
3.2	*-Norm	14
4.1	Patch Illustration [HÜ21]	21
5.1	Mesh tet_high	25
5.2	Mesh tet_low	25
5.3	Mesh hex	25
5.4	Geometry Adaption [WO+07a]	26
5.5	Illustration Venants Condition [KR19]	31
5.6	Venants Condition for tet_high Mesh	32
5.7	Venants Condition for hex Mesh	33
5.8	Venants Condition for tet_low Mesh	34
5.9	Comparison of Monopolar and Multipolar Venant, tet_high Mesh	35
5.10	Comparison of Monopolar and Multipolar Venant, hex Mesh	36
5.11	Comparison of Monopolar and Multipolar Venant, tet_low Mesh	37
5.12	Comparison of Dipole and Multipole, Tangential Dipoles, tet_high Mesh	41
5.13	Comparison of Dipole and Multipole, Tangential Dipoles, hex Mesh	42
5.14	Comparison of Dipole and Multipole, Tangential Dipoles, tet_low Mesh	43
5.15	Comparison of Dipole and Multipole, Radial Dipoles, tet_high Mesh	45
5.16	Comparison of Dipole and Multipole, Radial Dipoles, hex Mesh	47
5.17	Comparison of Dipole and Multipole, Radial Dipoles, tet_low Mesh	48
5.18	Ellipsoids for tet_high Mesh	52
5.19	Ellipsoids for hex Mesh	53
5.20	Ellipsoids for tet_low Mesh	54
5.21	Ellipsoids for Computed Quadrupoles	55

## List of Tables

5.1	Sphere Model	26
5.2	Mesh Parameters	26
5.3	Patches	39
5.4	$L_2$ -norm of Optimized Quadrupolar Moments	40
5.5	Quadrupolar Moments	49
5.6	Eigenvectors and -values	51

# 1 Introduction

The human brain has been a research topic of central relevance for a long time. As it is such a complex organ, there are still many open or only partially answered questions. Technologies that provide a way to localize brain activity are still being developed or known approaches are being improved. There are many diseases which benefit from a more accurate localisation. For example in pre-surgical epilepsy diagnosis it is very important to find the epileptogenic zone as accurately as possible, so that it can be removed without damaging any other important areas of the brain. There are many different technologies to study the human brain with. Some of them create images of the anatomy of the head, e.g. *X-ray computed tomography* (CT) or *magnetic resonance imaging* (MRI). Others can observe the characteristics of metabolism, e.g. *positron emission tomography* (PET), *single photon emission computed tomography* (SPECT) or *functional magnetic resonance imaging* (fMRI). A non-invasive way to measure the simultaneous activity of patches of neurons on a millisecond timescale is provided by *electroencephalography* (EEG) and *magnetoencephalography* (MEG). In order to use EEG and MEG for localizing brain activity an inverse problem has to be solved. This cannot be done analytically, but requires the solving of the corresponding forward problem.

In this thesis we will consider different ways to solve the EEG forward problem using the Principle of Saint Venant. The EEG forward problem plays an important role in the process of accurate localization, which is why we will invest in improving the solution of this problem. We will start giving a short overview of the physiological basics of the human brain in order to get a basic understanding about how a signal is produced. Afterwards we will see an introduction to the mathematical modeling of brain activity and the *finite element method* (FEM). The finite element method provides a way to numerically solve partial differential equations.

In order to be able to apply the FEM to the EEG forward problem, we have to investigate the way of modeling the source. The frequently used mathematical point dipole has a singularity and therefore cannot be handled directly. We will avoid this singularity by modeling the source as a monopole distribution. In order to do so, we will make use of the *Principle of Saint Venant*. In chapter 3 we will introduce this different way to model the source and look at approaches that use it. At first we will introduce a rather recent approach, the *multipolar Venant approach*, which has been developed by [HA19] and [VO+19]. It provides a possibility to compute the monopole distribution making use of a multipole expansion. After that we will have a look at the well-known *monopolar Venant approach*. The monopolar Venant approach provides another possibility to compute the monopole strengths. Next to the commonly used monopolar Venant approach without mixed moments we will also have a look at the monopolar approach with mixed moments, which has been introduced by [NÜ18].

After presenting the approaches, we will see that the multipolar Venant approach cannot only handle dipolar moments but also multipolar moments, which means that we can add quadrupoles. This may provide a way to better approximate extended sources. In chapter 4 we will look at how we can add these quadrupolar moments to our computational algorithm. Additionally we will define patches of activity which we will use to test the accuracy of modeling extended sources by the dipolar and the multipolar model.

At the end, in chapter 5, we will perform some tests in a 4-layer-sphere model. Therefore we will first of all introduce the used software, DUNEuro.

In a first experiment we will then perform some tests to find the best parameters for the multipolar Venant approach. In the second experiment we will use these parameters for the multipolar Venant approach and the monopolar Venant approaches and compare them to each other. In the last experiments we will then use our defined patches and test how much

the use of quadrupolar moments additionally to dipolar moments can improve the approximation of extended sources. We will look at optimized and computed quadrupolar moments, compare the performance of these two approaches and see how the resulting quadrupolar moments differ.

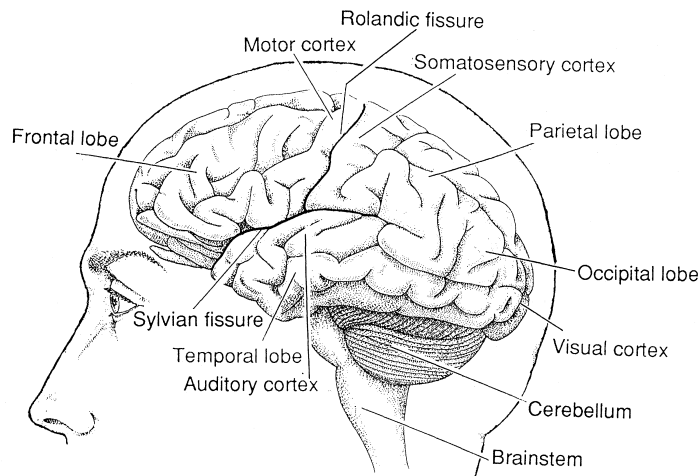


Figure 2.1: Human brain seen from the left side. Some of the important structural landmarks and special areas of the cerebral cortex are indicated. [HÄ+93]

## 2 The EEG Forward Problem

In order to understand the EEG and MEG data we want to investigate in this thesis, one has to understand basic working processes in the human brain. In the first section we will see how electric or magnetic potentials in the brain are created. Later on we will look at the mathematical modeling of these potentials. In the last part we will introduce a way to numerically solve the EEG forward problem, the finite element method. This chapter is geared to the elaborations by [HÄ+93], [HA19] and [VO11].

### 2.1 Physiological Basics

In figure 2.1 you can see a human brain viewed from the left side with some anatomical features identified. In EEG and MEG we are mostly interested in the uppermost layer of the brain, the cerebral cortex, which is a 2-4 mm thick sheet of gray tissue [HÄ+93]. One essential part of the brain are the neurons, which are concentrated in the gray matter. The human brain consists of  $86 \pm 8$  billions of these neurons, which are clustered in areas with unique responsibilities in processing on information and controlling the body. The areas responsible for each task are often assumed to be similar for individual human-beings, only the persons handedness seems to make a strong difference [HA19]. Neurons have the task to process informations in the human brain. In order to communicate among each other, they use electrochemical signaling. This process creates a measurable electric and magnetic potential.

Neurons consist of a cell body (soma), the dendrites, which are threadlike extensions, and the axon, a single long fiber arising at the axon hillock, see figure 2.2. The soma contains the nucleus and much of the metabolic machinery. The dendrites are receiving signals from other neurons and the axon has the task to carry the nerve impuls away from the soma to other cells.

Signal transfer along an axon is based on the ability of the membrane to alter its permeability to ions and the thus created rise and fall of electric potentials. The change is due to the opening of voltage-sensitive ion-channels as a result of an approaching action potential. This process leads to intra- and extracellular ion currents. Following Maxwell's equations of electrodynamics, the movement of electric charges results in electromagnetic

## Neuron

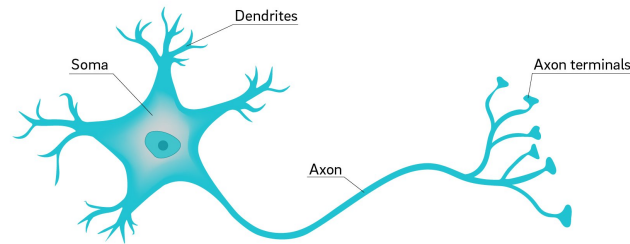


Figure 2.2: Illustration of a Neuron. [BA+18]

fields.

If the voltage at the axon hillock has reached a certain value, an *action potential* is initiated. Then the neuron “fires” and gives the signal to its neighboring neurons. This is done by a sudden change of the membran potential consisting in an abrupt rise followed by a fall of the same amplitude. The action potential then spreads along the axon and causes potential changes in the neighboring neurons, the *post-synaptic* neurons. This potential change (or the sum of various of these potential changes) may initiate an action potential again, which would mean the signal is passed on.

Since action potentials are too short (0.5 - 2 ms, [VO11]), not synchronized enough and their far-field induced by the resulting ion currents is dominated by the quadrupole term, they do not evoke a measurable EEG signal. Contrary to the action potential, the post synaptic potentials are simultaneous generated at different neurons. They last for tens of milliseconds at some ten-thousands neighboring and similarly oriented neurons, which build a patch of a few square millimeters of cortex surface [VO11]. This potential is strong enough to produce measurable electric potential differences at the headsurface which can be detected by EEG sensors. On top of that, there is a magnetic field generalized by the electric current, which can be measured by MEG sensors.

## 2.2 Mathematical Modeling

As we know now that there is electric current in the brain, we want to look at Maxwell's equations, see [MA65]. With the help of these equations we can calculate the electric potential and magnetic field.

$$\begin{aligned}
 \nabla \cdot E &= \frac{\rho}{\epsilon_0} \\
 \nabla \times E &= -\frac{\partial B}{\partial t} \\
 \nabla \cdot B &= 0 \\
 \nabla \times B &= \mu_0 \left( J + \epsilon_0 \frac{\partial E}{\partial t} \right).
 \end{aligned} \tag{2.1}$$

Here  $E$  is the electric field,  $\rho$  the electric charge density,  $\epsilon_0$  the electric constant,  $B$  the magnetic field,  $\mu_0$  the magnetic constant and  $J$  is the current density. Following [HÄ+93], and due to the low frequency regime, we can use the quasi-static approximation of Maxwell's equations. This means that in the calculations of  $E$  and  $B$ ,  $\frac{\partial E}{\partial t}$  and  $\frac{\partial B}{\partial t}$  can be ignored as source terms. So we get:

$$\begin{aligned}
 \nabla \cdot E &= \frac{\rho}{\epsilon_0} \\
 \nabla \times E &= 0 \\
 \nabla \cdot B &= 0 \\
 \nabla \times B &= \mu_0 J
 \end{aligned} \tag{2.2}$$

Since  $\nabla \times E$  is zero, the electric field can be represented as a gradient field, i.e.  $E = -\nabla u$  for an electric potential  $u$ .

On top of that, in bioelectromagnetism, the current density  $J$  produced by neuronal activity is split into two parts:

$$J = J^p + \sigma E. \tag{2.3}$$

Here  $J^p$  is the primary current and  $\sigma E$  is the volume or return current with  $\sigma$  as an electric conductivity tensor. The primary current can be seen as the main source of electric activity. The volume or return current is the result of the macroscopic electric field on charge carriers in the conducting medium. In order to localize the source of brain activity, we have to find the primary current.

Inserting the electric potential leads to

$$J = J^p - \sigma \nabla u. \tag{2.4}$$

With this we can rewrite the last equation of (2.2) to

$$\nabla \times B = \mu_0 (J^p - \sigma \nabla u). \tag{2.5}$$

Now we are taking the divergence. As the divergence of the curl is zero, we get

$$\nabla \cdot \sigma \nabla u = \nabla \cdot J^p. \tag{2.6}$$

We want to use this to formulate the EEG inverse and forward problem. Additionally, we need some definitions.

**Definition 2.1.** Let  $\Omega \subset \mathbb{R}^3$  be a domain,  $\sigma(x) : \Omega \rightarrow \mathbb{R}^{3 \times 3}$  be symmetric, positive and bounded with  $\sigma(x) \in L_\infty(\Omega)$  and  $X_{sens} \in \partial\Omega$  a set of discrete points at the boundary of  $\Omega$ .

Here  $\Omega$  represents the head domain and  $\sigma(x)$  is an electric conductivity tensor representing the conductivities of the different components of the human head. Following [HA19], we can assume the defined properties of the functional to be conformed. The set  $X_{sens}$  represents the sensor positions at the headsurface.

Using the results from Maxwell's equations we can formulate the EEG inverse problem.

**Problem 2.2** (EEG Inverse Problem). *Let  $\Omega, \sigma$  and  $X_{sens}$  be like in definition 2.1. Let the scalar potential be  $u : \Omega \rightarrow \mathbb{R}$ . The EEG inverse problem is to find neural activity  $J : \Omega \rightarrow \mathbb{R}$  which fulfills that*

$$\begin{aligned} \nabla \cdot (\sigma \nabla u) &= J \quad \text{in } \Omega, \\ \sigma \nabla u \cdot n &= 0 \quad \text{on } \partial\Omega. \end{aligned} \tag{2.7}$$

Let  $u|_{x_{sens}} := u_{sens}$  be given.

The problem says that we have measured an electric potential at the EEG sensors and then want to find the underlying sources in the brain that generated this potential. In a realistic model of the human brain this problem cannot be solved analytically. To solve it anyway, we have to solve the correspondent forward problem. That is to compute the expected potentials at the sensor positions for many different source locations in the brain. These potentials are saved in a so-called lead field matrix. Then there are different inverse solutions such as dipole fit or current density reconstruction methods that can be used to reconstruct possible inverse solutions. In order to get good inverse solutions, it is therefore very important to have good forward solutions. Also, as there have to be solved quite many forward computations, it is important to find a quick way to do so. Hence we will invest in finding an optimized way to solve the forward problem.

**Problem 2.3** (EEG Forward Problem). *Let  $\Omega \subset \mathbb{R}^3$  and  $\sigma(x) : \Omega \rightarrow \mathbb{R}^3$  be like in definition 2.1. The EEG forward problem is to find the scalar potential  $u : \Omega \rightarrow \mathbb{R}$  which solves the equation*

$$\begin{aligned} \nabla \cdot (\sigma \nabla u) &= J \quad \text{in } \Omega \\ \sigma \nabla u \cdot n &= 0 \quad \text{on } \partial\Omega, \end{aligned} \tag{2.8}$$

where  $J$  is the model for a given neuronal activity in the brain.

A common used model for the neuronal activity in the brain is the mathematical point dipole [DM+88]. The mathematical dipole is a point source with a location and a direction and can be expressed by a Dirac delta distribution. Let  $x_0$  be the location of the dipole and  $\vec{M} \in \mathbb{R}^3$  its moment. Then we can rewrite  $J(x)$  as

$$J(x) = \nabla \cdot \left( \vec{M} \delta_{x_0}(x) \right). \tag{2.9}$$

The mathematical dipole has shown to be a “good enough” approximation for many applications, but in certain scenarios like in epilepsy it might get important that, in fact, a biological electrical source has a physical extend and is no point singularity. Therefore we want to consider another approach to model the right hand side later on, which might be even more realistic. Furthermore, we will check if the use of multipolar sources can improve the approximation of extended sources.

## 2.3 Finite Element Method

There are many different approaches to solve the EEG forward problem, like the boundary element method ([AC+10], [GR+11], [MO+99], [ST+12]), the finite difference method ([MO+14], [VA+09], [WE+08]) or the finite volume method ([CO+06]). The finite element method, which we will present here, has some advantages over the others. For example it can treat geometries of arbitrary complexity, it has the possibility to consider material properties on a node-to-node or element-to-element basis and it has a very high accuracy, especially in the treatment of Neumann boundary conditions, which are important in the application considered [BU+97]. The FEM Theory is based on a *variational formulation* of the original partial differential equation. In the variational formulation, a solution is searched for in a so-called *Sobolev spaces*, which we will introduce in this section. In order to solve the variational problem numerically, we are going to use finite dimensional subspaces, *finite element spaces*. With the definitions of the finite element method we mainly follow the ideas of [BR13].

In order to give a short overview of the FEM theory, we are going to look at a general problem.

**Problem 2.4.** *Let  $\Omega$  be an open domain and  $\sigma : \Omega \rightarrow \mathbb{R}$  be positive and bounded. Find  $u : \Omega \rightarrow \mathbb{R}$  which solves*

$$\begin{aligned} \nabla \cdot (\sigma \nabla u) &= f \quad \text{in } \Omega \\ \sigma \nabla u \cdot n &= 0 \quad \text{on } \partial\Omega, \end{aligned} \tag{2.10}$$

for  $f \in L_2(\Omega)$ .

Classical solutions, i.e. solutions with conditions like being differentiable sufficiently often, can only be found under strong assumptions. This means that e.g.  $\sigma$  has to be a continuous conductivity, which is not true in our scenario. In order to find a solution anyway, one can use a variational formulation of the problem. Therefore we need the theory of Sobolev spaces. Sobolev spaces are based on the theory of weak derivatives so we have to define them at first. Let  $L_{loc}^1(\Omega)$  be the space of locally summable functions, see [?]

**Definition 2.5** (Weak Derivative). *Suppose  $u, v \in L_{loc}^1(\Omega)$  and  $\alpha = (\alpha_1, \dots, \alpha_n)$  is a multi-index of order  $|\alpha| = \alpha_1 + \dots + \alpha_n = k$ . We say the  $v$  is the  $\alpha$ -th-weak partial derivative of  $u$ , written*

$$D^\alpha u = \frac{\partial^{\alpha_1}}{\partial x_1^{\alpha_1}} \dots \frac{\partial^{\alpha_n}}{\partial x_n^{\alpha_n}} u = v,$$

provided

$$\int_{\Omega} u D^\alpha \phi \, dx = (-1)^{|\alpha|} \int_{\Omega} v \phi \, dx$$

for all test functions  $\phi \in C_0^\infty(\Omega)$ .

With the help of weak derivatives we can define Sobolev spaces.

**Definition 2.6** (Sobolev Spaces). *For  $m \in \mathbb{N}_0$  the Sobolev space  $H^m(\Omega)$  is the set of all functions  $u \in L_2(\Omega)$  with a weak derivative  $D^\alpha u$  for all  $|\alpha| \leq m$ . The scalar product is defined by*

$$(u, v)_m := \sum_{|\alpha| \leq m} \langle D^\alpha u, D^\alpha v \rangle,$$

and the corresponding norm is

$$\|u\|_m := \sqrt{(u, u)_m}.$$

Let  $H_0^m(\Omega)$  be the completion of  $C_0^\infty(\Omega)$  regarding the Sobolev norm  $\|\cdot\|_m$ .

For our purpose we need a test space which is a subset of  $H^1(\Omega)$ . We define the test space  $V$  as

$$V := \{v \in H^1(\Omega) : \nabla \cdot (\sigma \nabla v) \in H_0^1(\Omega) \text{ and } \sigma \nabla v \cdot n = 0 \text{ on } \partial\Omega\}.$$

Let  $v \in V$ . In order to obtain a variational formulation of the problem 2.4, we multiply both sides with  $v$ , integrate over  $\Omega$  and apply integration by parts to the left hand side.

**Problem 2.7** (Variational Formulation). *Find an  $u \in H^{-1}(\Omega)$  which fulfills*

$$\int_{\Omega} \sigma \nabla u \nabla v \, dx = \int_{\Omega} f v \, dx, \quad (2.11)$$

for all  $v \in V$ .

Here  $H^{-1}(\Omega)$  is the dual space to  $H_0^1(\Omega)$ . Since we use  $\sigma(x)$  from definition 2.1, the left hand side is positive, symmetrical and bounded. Therefore we have a bounded and thus continuous and coercive bilinearform. If  $f \in L_2(\Omega)$ , the right hand side is a linear functional.

Just like this, there will not be a unique solution to the problem. If there is a solution, it is only unique up to a constant. In order to get a unique solution, we add another condition following [HA19].

**Problem 2.8.** *Let  $\eta \in H_0^1(\Omega)$  be a function with  $\int_{\Omega} \eta \, dx = 1$ . Find  $u \in \{g \in H^{-1}(\Omega) : \int_{\Omega} \eta g \, dx = 0\}$  such that*

$$\int_{\Omega} \sigma \nabla u \nabla v \, dx = \int_{\Omega} f v \, dx \text{ for all } v \in V. \quad (2.12)$$

The solution  $u$  is then called the *weak solution*. In order to prove that there is a solution to Problem 2.8, we use the theorem (or lemma) of Lax Milgram.

**Theorem 2.9** (Lax-Milgram Theorem, [BR+07], Theorem 2.7.7). *Given a Hilbert-Space  $(V, (\cdot, \cdot))$ , a continuous and coercive bilinearform  $a(\cdot, \cdot)$  and a continuous linear functional  $F \in V'$ , there exists a unique  $u \in V$  such that*

$$a(u, v) = F(v) \text{ for all } v \in V. \quad (2.13)$$

In our case we can consider

$$a(u, v) := \int_{\Omega} \sigma \nabla u \nabla v \, dx,$$

with  $u \in \{g \in H^{-1}(\Omega) : \int_{\Omega} \eta g \, dx = 0\}$ ,  $v \in V$  as the bilinearform and

$$F(v) := \int_{\Omega} f v \, dx$$

as the linear functional. Then the Lemma of Lax-Milgram tells us that there is a unique solution  $u \in H^{-1}(\Omega)$  if  $f \in L_2(\Omega)$ .

Based on the presented mathematical foundation, we want to introduce a discretization method to numerically solve the EEG forward problem, the finite element method (FEM). We will follow the elaboration by [NÜ18].

The main idea is to replace the infinite dimensional space  $V$  with a finite dimensional space  $V_h$ . Instead of solving

$$a(u, v) = F(v) \quad \text{for all } v \in V$$

we are going to solve

$$a(u_h, v_h) = F(v_h) \quad \text{for all } v_h \in V_h$$

Here  $h$  is a discretization parameter such that the solution converges to the original solution if  $h \rightarrow 0$ . In order to get an idea about the accuracy of this approach, we will cite Céa's Lemma.

**Lemma 2.10** (Céa's Lemma, [BR+07], Theorem 2.8.1). *Given a Hilbert space  $(V, \langle \cdot, \cdot \rangle)$ , a continuous, coercive bilinear form  $a(\cdot, \cdot)$ , a continuous linear functional  $f \in V'$  and  $u \in V$  solving the weak formulation. For the solution  $u_h \in V_h$  of the finite element variational problem we have*

$$\|u - u_h\|_V \leq \frac{C}{\alpha} \min_{v \in V_h} \|u - v\|_V,$$

with  $C$  being the continuity constant and  $\alpha$  being the coercivity constant of  $a(\cdot, \cdot)$  on  $V$ .

The lemma shows that the accuracy of the finite element solution strongly depends on how the discrete function space is chosen to approximate the solution  $u$ . Therefore we will have a look at the construction of this discrete function space. The basis is a partition of the computational domain  $\Omega$ .

**Definition 2.11** (Tessellation). *A tessellation of a domain  $\Omega$  is a set  $\tau_h(\Omega) := \{E_0, \dots, E_{m-1}\}$  of open convex polytopes  $E_i \subset \Omega$  such that*

$$\begin{aligned} \bigcup_{i=0}^{m-1} \bar{E}_i &= \bar{\Omega} \quad \text{and} \\ E_i \cap E_j &= \emptyset, \quad i \neq j. \end{aligned}$$

A tessellation is called admissible if the following conditions are met:

1. If  $\bar{E}_i \cap \bar{E}_j$  consists of exactly one point, this point is a common vertex of  $E_i$  and  $E_j$ .
2. If  $\bar{E}_i \cap \bar{E}_j$  consists of more than one point for  $i \neq j$ , then  $\bar{E}_i \cap \bar{E}_j$  is a common edge or, in three dimensions, a common face of  $E_i$  and  $E_j$ .

A family of tessellations  $\{\tau_h\}$  is called shape-regular if there is a  $\kappa > 0$  such that every  $T$  in  $\tau_h$  contains a circle of radius  $\rho_T$  with

$$\rho_T \geq \frac{h_T}{\kappa},$$

where  $h_T$  denotes the diameter of  $T$ . A family of tessellations is called uniform, if every  $T$  in  $\tau_h$  contains a circle with radius  $\rho_T$  with

$$\rho_T \geq \frac{h}{\kappa},$$

with  $h := \max_{T \in \tau_h} h_T$ .

In this thesis we will look at admissible tessellations with tetrahedral or hexahedral polyhedrons. On such tessellations we define the finite element space  $V_h^k$ .

**Definition 2.12** (Finite Element Space). *The space  $V_h^k$  is defined as the space of continuous, piecewise polynomial functions, i.e.*

$$V_h^k := \{v_h \in C^0(\Omega) : v_h|_E \in P^k(E) \quad \forall E \in \tau_h(\Omega)\},$$

where  $P^k(E)$  denotes a space of polynomials of degree  $k \in \mathbb{N}$  on an element  $E$ .

This space is a conforming space, i.e.  $V_h^k \subset H^1(\Omega)$ , see [BR13, Theorem 5.2]. Usually, first order polynomials are employed, i.e. linear polynomials on tetrahedrons and multilinear polynomials on hexahedrons [NÜ18]. The basis functions  $\phi_i$  for the piecewise linear function space are chosen as the Lagrangian basis functions.

**Definition 2.13** (Lagrangian Basis Functions). *Let  $x_0, \dots, x_{N-1} \in \mathbb{R}^d$  denote the vertices of a tessellation  $\tau_h$ . The basis consisting of the linear functions  $\phi_i, i = 0, \dots, N - 1$  which fulfill the property*

$$\phi_i(x_j) = \begin{cases} 1 & , i = j \\ 0 & , i \neq j, \end{cases}$$

*is called Lagrangian basis.*

This would be a good way to solve our forward problem, but we still have to deal with the fact that the right hand side is too complicated. If we consider the neural activity as a mathematical dipole,  $J(x) \notin L_2(\Omega)$ . Therefore we have to use a regularization before we can use FE methods.

There are different ideas on how to deal with this problem using the mathematical dipole, see for example the partial integration approach ([YA+91], [WE+00]), the full and projected subtraction approach ([DR+09], [WO+07b], [BE18], [BE19]) and the Whitney approach ([PU+11], [PU+16], [TA+05], [BA+15], [MI+19]). We are going to use another way. We will not consider the mathematical point dipole but an approximation.

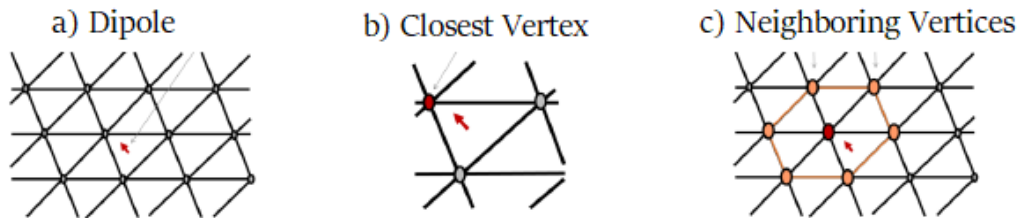


Figure 3.1: Choice of monopole locations in a 2D FEM mesh. [KR19]

### 3 Principle of Saint Venant

In this chapter we are going to present a way to model the source avoiding the point singularity caused by a mathematical point dipole. Afterwards we will introduce a relatively new approach to compute the forward problem with this model, the *multipolar Venant approach*. At the end of this section we will look at a well known approach to solve the problem using the introduced model, the *monopolar Venant approach*, which we want to compare with the multipolar Venant approach.

#### 3.1 Monopole Distribution

One idea on how to get rid of the singularity caused by a mathematical point dipole is to model the source in a different way. As the dipole has shown to be a good approximation of brain activity, we are going to try to create a similar potential with the new model. Here the idea to model the source is to place  $n \in \mathbb{N}$  monopoles on mesh vertices  $x_1, \dots, x_n \in \mathbb{R}^d$  close to the source location  $x_0 \in \mathbb{R}^d$ . The approach has first been developed by Richard Schöner and colleagues and published in [BU+97] and was known as the *blurred dipole approach*. Later on it has been used in many publications, e.g. [LE+09], [VO16], [WO+07a], [WO+07b], [ME15].

A common way to choose the monopoles is to find the monopole that lies closest to the dipole location and mark it as  $x_1$ . In the next step the vertices sharing an edge, a face or a volume with  $x_1$  are marked as  $x_2, \dots, x_n$  - this means, for tetrahedrons you get about 16 and for hexahedrons you get 27 monopoles [BU+97]. See figure 3.1 to find an example of this choice of the monopole locations in a 2D FEM mesh.

Following the principle of Saint Venant saying “specific details of load application (e.g. mathematical dipole or monopole distribution) do not influence the result observed some distance away from the locus of load application (i.e. the measured potential difference at the head surface)” [BU+97], the potential at the sensor positions can be similar for a monopole distribution around the source location and the point dipole at the source location. With regard to the underlying physiology, the monopole distribution might even be a more realistic source model than the point dipole. As explained before, activity in the brain has a certain extent. To measure a signal, there has to be a large number of active neurons, consisting of around  $10^5$  to  $10^7$  cells, laying in a small volume [ME15]. This extent cannot be represented by a point dipole. The monopole distribution, as it is distributed over some vertices, might represent the extent better. Later on we will have a closer look at extended sources and try to approximate them even more accurate with the use of quadrupolar moments.

With the monopole distribution we can rewrite the right hand side  $J$  as

$$J_m(x) = \sum_{i=1}^n q_i \delta_{x_i}(x), \quad (3.1)$$

with  $\delta_{x_i}$  the delta distribution at  $x_i$ . Here  $x_1, \dots, x_n \in \mathbb{R}^3$  are the monopole locations and  $q_1, \dots, q_n \in \mathbb{R}^3$  represent the strengths at each of these locations.

Then we can define the monopole distribution forward problem:

**Problem 3.1** (Monopole Distribution Forward Problem). *Let  $\Omega \subset \mathbb{R}^3$  and  $\sigma(x) : \Omega \rightarrow \mathbb{R}^{3 \times 3}$  be like in definition 2.1. Find the scalar potential  $u : \Omega \rightarrow \mathbb{R}$  which solves the equation*

$$\begin{aligned} \nabla \cdot (\sigma \nabla u) &= \sum_{i=1}^n q_i \delta_{x_i} \quad \text{in } \Omega, \\ \sigma \nabla u \cdot n &= 0 \quad \text{on } \partial\Omega. \end{aligned} \quad (3.2)$$

It can be proven that there is a unique solution to this problem, see [HA19].

For using the Finite Element Method, the right-hand-side can be discretized as [HA19]

$$J_m(x) = \sum_{i=1}^n (J_h)_i \cdot \phi_i(x),$$

with

$$(J_h)_j = \begin{cases} q_j, & \text{if } x_j \in \{x_1, \dots, x_n\} \\ 0, & \text{else.} \end{cases}$$

There are different ways to choose the monopole locations  $x_1, \dots, x_n$ . We will go on with the one described above except for one additional condition. We will see that in some test scenarios the solutions can be improved if we only consider monopole locations which are in the same conductivity layer as the source namely in grey matter, the so-called *Venant Condition* [ME15]. We will have a closer look at this in chapter 5.

Once the monopole locations are fixed, it will be our task to determine the strength  $q_i$ ,  $i = 1, \dots, n$ , at each monopole location, in order to optimally reproduce the moments of the source. In this thesis we will consider different ways to solve this problem and compare them.

### 3.2 Multipolar Venant Approach

In this section we will look at an approach to compute the monopole strengths  $q_1, \dots, q_n$ , the *multipolar Venant approach*. Following [HA19] and [VO+19], we are going to use multipole expansion to compute the moments of the monopole distribution. We will begin with a repetition of the forward problems for the mathematical point dipole and the monopole distribution.

**Problem 3.2** (Mathematical Point Dipole Forward Problem). *Find  $u_d$  for the mathematical dipole that solves the equations*

$$\begin{aligned}\nabla \cdot (\sigma \nabla u_d) &= \nabla \cdot (\vec{M} \delta_{x_0}(x)) \quad \text{in } \Omega, \\ \sigma \nabla u_d \cdot n &= 0 \quad \text{on } \partial\Omega.\end{aligned}$$

**Problem 3.3** (Monopole Distribution Forward Problem). *Find  $u_m$  for the monopole distribution that solves the equations*

$$\begin{aligned}\nabla \cdot (\sigma \nabla u_m) &= \sum_{i=1}^n q_i \delta_{x_i} \quad \text{in } \Omega, \\ \sigma \nabla u_m \cdot n &= 0 \quad \text{on } \partial\Omega.\end{aligned}$$

In these problems  $u_d$  and  $u_m$  symbolize the electric potential of the dipole and of a monopole distribution, respectively. We want to ensure that these potentials are the same. In order to simplify the comparison, we will use multipole expansion to expand the monopole distribution potential.

First of all we have to consider the fact that if the right hand side is assumed to have singularities, the potentials are not in the function space  $L_2(\Omega)$ . Therefore we cannot use the  $L_2$ -norm to measure the difference between the dipole potential and the monopole distribution potential. Following [HA19], we will develop another norm. For the development we assume the source position at the origin. We will get rid of this by subtracting the real source location at the end. We will start with an assumption.

**Assumption 3.4.** *Let  $x_1, \dots, x_n \in \Omega_h$  fulfill that a small ball around the source location  $x_0$  with radius  $\delta \in \mathbb{R}^{>0}$  exists such that*

$$x_1, \dots, x_n \in B_\delta(0) := \{x \in \Omega_h : |x| < \delta\},$$

and a  $\sigma_0 \in \mathbb{R}^{>0}$  such that

$$\sigma(x) = \sigma_0 \quad \text{for all } x \in B_\delta(0).$$

This means that we want to find a ball around the source location which contains all monopole locations and has the same conductivity in the whole region. Therefore the ball has to lie completely in one compartment of the headmodel. Out of this assumption we can define some parameters which will be used for the required norm.

**Definition 3.5.** *Define  $\delta_0$  as the maximal  $\delta \in \mathbb{R}$  such that assumption 3.4 holds and*

$$\delta_1 := \inf \{ \delta \in \mathbb{R} : \delta_0 \geq \delta_1 > \max\{|x_1|, \dots, |x_n|\} \}.$$

See figure 3.2 to get an idea how it could look like in 2D. Additionally let  $\sigma_0 \in \mathbb{R}^{>0}$  be as in assumption 3.4.

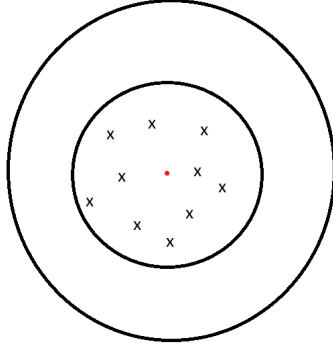


Figure 3.2: Let the red dot be the origin and the x the monopole locations. Then  $\delta_1$  would be the radius of the inner circle and  $\delta_0$  the radius of the outer circle.

As we do not have the goal to estimate the error at the dipole and monopole locations, we are more interested in choosing the parameters in a way that the difference between the dipolar source and the monopolar source distribution at the EEG sensor positions, which are located at the surface of the domain,  $\partial\Omega$ , is minimal. Also we are only able to estimate the error on the surface of the small ball around the dipole location where there is the same conductivity [HA19]. In order to do so, we choose our norm

$$\|v\|_* := \|v\|_{L_2(B_{\delta_0}(0) \setminus B_{\delta_1}(0))}.$$

This norm we are going to use to measure the difference between the dipole potential and the monopole distribution potential. Prior to that we will look at the dipole and monopole distribution potential again. In infinite space with homogeneous conductivity the potential of the dipole can be represented by the fundamental solution

$$\Phi_D(x) = \frac{1}{4\pi\sigma_0} \cdot \frac{\langle \vec{M}, x \rangle}{|x|^3}. \quad (3.3)$$

This is a pure dipole potential and cannot be expanded further. Every moment except the dipole moment is zero. In order to be able to easily compare this potential to the monopole distribution potential, we use multipole expansion for the latter. The multipole expansion is based on a Taylor expansion of the electric field evoked by a charge distribution  $\rho$ . An electric potential  $\Phi$  evoked by a general charge distribution  $\rho$  can be computed as [JA99]

$$\Phi(x) = \frac{1}{4\pi\sigma_0} \int_{\Omega} \frac{\rho(x')}{\|x - x'\|} dx'. \quad (3.4)$$

If we apply our discrete source distribution,  $J_m = \sum_{i=1}^n q_i \delta_{x_i}$ , for the potential of the monopole distribution we get

$$\Phi_M(x) = \frac{1}{4\pi\sigma_0} \cdot \sum_{i=1}^n \frac{q_i}{\|x - x_i\|_2}. \quad (3.5)$$

Following [JA99] and assuming  $|x_i| < |x|$ , which is given as we only consider locations  $x$  at the surface of the domain, it holds that

$$\frac{1}{\|x - x_i\|_2} = \sum_{l=0}^{\infty} \frac{|x_i|^l}{|x|^{l+1}} \mathcal{P}_l(\cos(\theta_i)). \quad (3.6)$$

Here  $\theta_i$  is the angle between  $x_i$  and  $x$  and  $\mathcal{P}_l(x)$ ,  $l = 0, 1, 2, \dots$ , are the Legendre Polynomials, i.e.

$$\begin{aligned}\mathcal{P}_0(x) &= 1, \\ \mathcal{P}_1(x) &= x, \\ \mathcal{P}_2(x) &= \frac{1}{2}(3x^2 - 1), \\ &\dots\end{aligned}$$

Inserting this in (3.5) leads to the multipole expansion for the monopole distribution potential:

$$\Phi_M(x) = \frac{1}{4\pi\sigma_0} \sum_{l=0}^{\infty} \sum_{i=1}^n \frac{q_i \cdot |x_i|^l}{|x|^{l+1}} \mathcal{P}_l(\cos(\theta_i)). \quad (3.7)$$

Computing the strength of the monopole distribution such that the potential is the same as the dipole potential would lead to the following problem. As a difference measure we use the \*-norm.

**Problem 3.6.** *Given are the monopole locations  $x_1, \dots, x_n$  and the dipole potential  $\Phi_D$ . Compute  $q_1, \dots, q_n$  such that*

$$\|\Phi_D - \Phi_M\|_* = \min_{\tilde{q}_1, \dots, \tilde{q}_n} \left\| \frac{1}{4\pi\sigma_0} \cdot \frac{\langle \vec{M}, x \rangle}{|x|^3} - \frac{1}{4\pi\sigma_0} \sum_{l=1}^{\infty} \sum_{i=1}^n \frac{\tilde{q}_i \cdot |x_i|^l}{|x|^{l+1}} \mathcal{P}_l(\cos(\theta_i)) \right\|_*.$$

The norm can be minimized by comparing the coefficients of both expansions. Unfortunately, this requires to solve an infinite sum of equations. Thus we have to find a way to reduce this problem and make it solveable.

### 3.3 Computational Algorithm

Our aim is to reduce the problem to a finite number of calculations. Then we are able to generate a computable algorithm. Therefore we follow the concept of [HA19] and [VO+19]. The idea is to only consider the terms up to second order moments. The terms within the multipole expansion decay with at least  $\frac{1}{\sigma_0^3}$  and hence it is reasonable to cut the expansion after the third term [HA19]. With this assumption the problem reduces to find  $q_1, \dots, q_n$  such that

$$\left\| \Phi_D - \underbrace{\frac{1}{4\pi\sigma_0} \sum_{l=0}^2 \sum_{i=1}^n \frac{q_i \cdot |x_i|^l}{|x|^{l+1}} \mathcal{P}_l(\cos(\theta_i))}_{=: \tilde{\Phi}_M(x)} \right\|_* \rightarrow \min.$$

With the definition of the scalar product and with

$$\cos(\theta_i) = \frac{x \cdot x_i}{|x||x_i|},$$

we can split  $\tilde{\Phi}_M(x)$  into single terms for each moment order.

$$\begin{aligned} \tilde{\Phi}_M(x) &= \frac{1}{4\pi\sigma_0|x|} \sum_{i=1}^n q_i \\ &+ \frac{1}{4\pi\sigma_0|x|^2} \left\langle \sum_{i=1}^n q_i x_i, \frac{x}{|x|} \right\rangle \\ &+ \frac{1}{4\pi\sigma_0 2|x|^3} \left\langle \frac{x}{|x|}, \frac{\sum_{i=1}^n q_i (3x_i \otimes x_i - |x_i|^2 I_{3 \times 3})}{2} \frac{x}{|x|} \right\rangle, \end{aligned}$$

with  $I_{3 \times 3} \in \mathbb{R}^{3 \times 3}$  being the identity matrix. Looking at the dipole potential, we notice that it only contains the moments of first order - all other terms are zero. If we insert this, we get the following conditions for the monopole distribution potential:

$$\begin{aligned} 0 &= \frac{1}{4\pi\sigma_0|x|} \sum_{i=1}^n q_i \\ \frac{1}{4\pi\sigma_0} \frac{\langle \vec{M}, x \rangle}{|x|^3} &= \frac{1}{4\pi\sigma_0|x|^2} \left\langle \sum_{i=1}^n q_i x_i, \frac{x}{|x|} \right\rangle \\ 0 &= \frac{1}{4\pi\sigma_0 2|x|^3} \left\langle \frac{x}{|x|}, \frac{\sum_{i=1}^n q_i (3x_i \otimes x_i - |x_i|^2 I_{3 \times 3})}{2} \frac{x}{|x|} \right\rangle. \end{aligned}$$

Based on the fact that these conditions have to hold for all  $x \in \Omega$ , they can be transformed into equations independent from  $x$ :

$$\begin{aligned} 0 &= \sum_{i=1}^n q_i \\ \vec{M} &= \sum_{i=1}^n q_i x_i \\ \mathbf{0}_{3 \times 3} &= \sum_{i=1}^n q_i (3x_i \otimes x_i - |x_i|^2 I_{3 \times 3}) \end{aligned}$$

In order to get rid of our assumption that the source location is in the origin, we replace  $x_i$  by

$$\Delta x_i := x_i - x_0,$$

for all  $i = 1, \dots, n$ .

We can interpret these conditions as linear equations of  $q_1, \dots, q_n$  and thus we can write the conditions in vector-matrix-notation. In order to improve the conditions of the linear system, we need a scaling factor  $a^{ref}$  so that  $\frac{x_{ij}}{a^{ref}} < 1$  holds for all  $i = 1, \dots, n, j = 1, 2, 3$ . The scaled variables will be indicated by the bar. We get

$$\underbrace{\begin{pmatrix} 0 \\ \bar{m}_1 \\ \bar{m}_2 \\ \bar{m}_3 \\ 0 \\ \vdots \\ 0 \end{pmatrix}}_{=:\vec{t}} = \underbrace{\begin{pmatrix} 1 & 1 & \dots & 1 \\ \Delta\bar{x}_{11} & \Delta\bar{x}_{21} & \dots & \Delta\bar{x}_{n1} \\ \Delta\bar{x}_{12} & \Delta\bar{x}_{22} & \dots & \Delta\bar{x}_{n2} \\ \Delta\bar{x}_{13} & \Delta\bar{x}_{23} & \dots & \Delta\bar{x}_{n3} \\ 3 \cdot \Delta\bar{x}_{11}^2 - \|\Delta\bar{x}_1\|_2^2 & 3 \cdot \Delta\bar{x}_{21}^2 - \|\Delta\bar{x}_2\|_2^2 & \dots & 3 \cdot \Delta\bar{x}_{n1}^2 - \|\Delta\bar{x}_n\|_2^2 \\ 3 \cdot \Delta\bar{x}_{12}^2 - \|\Delta\bar{x}_1\|_2^2 & 3 \cdot \Delta\bar{x}_{22}^2 - \|\Delta\bar{x}_2\|_2^2 & \dots & 3 \cdot \Delta\bar{x}_{n2}^2 - \|\Delta\bar{x}_n\|_2^2 \\ 3 \cdot \Delta\bar{x}_{13}^2 - \|\Delta\bar{x}_1\|_2^2 & 3 \cdot \Delta\bar{x}_{23}^2 - \|\Delta\bar{x}_2\|_2^2 & \dots & 3 \cdot \Delta\bar{x}_{n3}^2 - \|\Delta\bar{x}_n\|_2^2 \\ 3 \cdot \Delta\bar{x}_{11} \cdot \Delta\bar{x}_{12} & 3 \cdot \Delta\bar{x}_{21} \cdot \Delta\bar{x}_{22} & \dots & 3 \cdot \Delta\bar{x}_{n1} \cdot \Delta\bar{x}_{n2} \\ 3 \cdot \Delta\bar{x}_{12} \cdot \Delta\bar{x}_{13} & 3 \cdot \Delta\bar{x}_{22} \cdot \Delta\bar{x}_{23} & \dots & 3 \cdot \Delta\bar{x}_{n2} \cdot \Delta\bar{x}_{n3} \\ 3 \cdot \Delta\bar{x}_{13} \cdot \Delta\bar{x}_{11} & 3 \cdot \Delta\bar{x}_{23} \cdot \Delta\bar{x}_{21} & \dots & 3 \cdot \Delta\bar{x}_{n3} \cdot \Delta\bar{x}_{n1} \end{pmatrix}}_{=:V} \cdot \underbrace{\begin{pmatrix} q_1 \\ q_2 \\ \vdots \\ q_n \end{pmatrix}}_{=:\vec{q}}. \quad (3.8)$$

We can compute  $\vec{q}$  by minimizing the functional

$$F(\vec{q}) = \|V \cdot \vec{q} - \vec{t}\|_2^2 \rightarrow \min.$$

In general the number of degrees of freedom  $n$  is larger than the number of determined parameters on the left hand side. Hence there is no unique solution to the minimization problem. In this case we will use a Tikhonov regularization and look for a solution with low energy. This means that high spatial frequency components in the  $q$ -vector shall be penalized [HA19]. In order to achieve this, we choose a regularisation parameter  $0 < \lambda < 1$ , a weighting exponent  $r$  and a matrix  $W \in \mathbb{R}^{n \times n}$  with

$$W = \begin{pmatrix} \|\Delta\bar{x}_1\|_2^r & 0 & \dots & 0 \\ 0 & \|\Delta\bar{x}_2\|_2^r & \ddots & \vdots \\ \vdots & \ddots & \ddots & 0 \\ 0 & \dots & 0 & \|\Delta\bar{x}_n\|_2^r \end{pmatrix}$$

Following [VO+19], we will set the weighting exponent to  $r = 1$ . With this we can consider a new functional

$$F_\lambda(\vec{q}) = \|\vec{t} - V \cdot \vec{q}\|_2^2 + \lambda \|W \cdot \vec{q}\|_2^2.$$

Minimizing  $F_\lambda(\vec{q})$  will lead to a unique solution. The regularisation parameter  $\lambda$  indicates how much  $q_1, \dots, q_n$  will be smoothed. It can be chosen arbitrarily, but its choice affects the results. In [HA19] it has been shown that a  $\lambda$  in the range of  $10^{-4}$  to  $10^{-10}$  is a good choice.

### 3.4 Error Estimation

Having this approach, one could ask how suitable this way of using a monopole distribution instead of a mathematical dipole is. In [HA19] an error estimation has been proven, which we just want to cite here.

**Theorem 3.7.** *Let assumption 3.4 hold,  $x_1, \dots, x_n$  be the monopole locations and  $q_1, \dots, q_n$  fulfill the conditions*

$$\begin{aligned} 0 &= \sum_{i=1}^n q_i, \\ \vec{M} &= \sum_{i=1}^n q_i x_i, \\ 0_{3 \times 3} &= \sum_{i=1}^n q_i (3x_i \otimes x_i - |x_i|^2 I_{3 \times 3}). \end{aligned}$$

Then the error between the potential of the monopole distribution  $\Phi_M(x)$  and the potential of the dipole  $\Phi_D(x)$  is

$$\|\Phi_D(x) - \Phi_M(x)\|_* \leq C \frac{1}{\delta_0} \left( \frac{1}{1 - \frac{|x_{max}|}{\delta_0}} \right),$$

with  $x_{max} := \max\{|x_i| : i = 1, \dots, n\}$ ,  $C \in \mathbb{R}$  and  $C = C(\sigma_0, n, q_{max}, \Omega)$ .

This error estimation cannot be used like this in an EEG forward setting. A realistic setting will have conductivity jumps which are not covered by this error estimation. Nonetheless, we can use this estimation to get a better understanding of the multipolar Venant approach. It shows that the error decreases when the difference between  $|x_{max}|$  and  $\delta_0$  increases. This means that for a scenario of computing on uniform conductivity, the error is maximal at the border of  $B_{|x_{max}|}(x_0)$  and decreases towards the border of the domain where we are computing on. This means the error would be minimal at the sensor positions, which are located at the border of the domain.

For a scenario in which we include several layers with different conductivities, which is more realistic, we can achieve a big difference between  $|x_{max}|$  and  $\delta_0$  by ensuring that the area of possible monopole distribution is as small as possible and the area of uniform conductivity is as big as possible. As the area of uniform conductivity is determined by the head model, we cannot control this part. However, we can control the area of monopole distribution by changing the grid resolution. The higher the resolution, the smaller the area of monopole locations. If the grid is coarser, the area where monopoles are placed is widened and so the distance to the next conductivity jump is decreased. Thus we can deduce the importance of a high grid resolution from this error estimation.

### 3.5 Monopolar Venant Approach

The *monopolar Venant approach*, also known as the *blurred dipole approach*, is another well known possibility to solve the EEG monopole distribution forward problem. Again we want to find the strength  $q_1, \dots, q_n$  for the monopoles at the locations  $x_1, \dots, x_n$ , but this approach does not use multipole expansion. Here we will follow the ideas of [VO16], [NÜ18] and [WO+07a], which are all based on the ideas of [BU+97]. We want to introduce two variations of the monopolar Venant approach. Later in chapter 5 we will compare these two approaches to the multipolar Venant approach.

Instead of computing the monopole distribution potential following the multipole expansion as

$$\Phi_M(x) = \frac{1}{4\pi\sigma_0} \sum_{l=0}^{\infty} \sum_{i=1}^n \frac{q_i \cdot |\Delta x_i|^l}{|x|^{l+1}} \mathcal{P}_l(\cos(\theta_i)), \quad (3.9)$$

(compare equation (3.7)), here it is computed as

$$\Phi_{Mono}(x) = \frac{1}{4\pi\sigma_0} \sum_{l=0}^{N_m} \sum_{i=1}^n q_i (\Delta x_i)^l. \quad (3.10)$$

This way of computing the moments is a consequence of the historical derivation of the Venant approach [VO16]. Here  $N_m \in \mathbb{N}$  represents the number of moments and again, in order to get a computable algorithm, we will only consider the terms up to  $N_m = 2$ . This leads to the following conditions

$$\begin{aligned} 0 &= \sum_{i=0}^n q_i \\ \vec{M} &= \sum_{i=0}^n q_i \Delta x_i \\ \vec{0} &= \sum_{i=0}^n q_i (\Delta x_i)^2 \end{aligned}$$

We see that the first four conditions are the same as for the multipolar Venant approach. Only the equation for  $l = 2$  is different.

We can rewrite the problem in matrix-vector notation. We need a vector  $\vec{t}$  with

$$\vec{t} = \begin{pmatrix} 0 \\ m_1 \\ m_2 \\ m_3 \\ 0 \\ \vdots \\ 0 \end{pmatrix}$$

where  $m_1, m_2, m_3 \in \mathbb{R}$  are the moments in each spatial direction and either  $\vec{t} \in \mathbb{R}^7$  for the monopolar Venant approach without mixed moments or  $\vec{t} \in \mathbb{R}^{10}$  for the monopolar Venant approach with mixed moments. We will take a closer look at these two cases further down below. Furthermore, we need a vector  $\vec{q} \in \mathbb{R}^n$  containing the monopole loads

$$\vec{q} = \begin{pmatrix} q_1 \\ q_2 \\ \vdots \\ q_n \end{pmatrix}$$

On top of that, we need a matrix  $V \in \mathbb{R}^{m \times n}$  with

$$V(j, i) = (\Delta x_i)^{\alpha_j},$$

$i = 1, \dots, n$  and  $\alpha_1, \dots, \alpha_m \in \mathbb{N}_0^3$  a set of multi-indices, where

$$(\Delta x_i)^{\alpha_j} = (\Delta x_i)_1^{\alpha_{j1}} \cdot (\Delta x_i)_2^{\alpha_{j2}} \cdot (\Delta x_i)_3^{\alpha_{j3}}.$$

For the monopolar Venant approach without mixed moment, the multi-indices are chosen as the zero vector and the vectors consisting of a single non-zero entry  $l \in \mathbb{N}$  with  $l \leq N_m$ , i.e.

$$\underbrace{\begin{pmatrix} 0 \\ 0 \\ 0 \end{pmatrix}}_{\alpha_1}, \underbrace{\begin{pmatrix} 1 \\ 0 \\ 0 \end{pmatrix}}_{\alpha_2}, \underbrace{\begin{pmatrix} 0 \\ 1 \\ 0 \end{pmatrix}}_{\alpha_3}, \underbrace{\begin{pmatrix} 0 \\ 0 \\ 1 \end{pmatrix}}_{\alpha_4}, \underbrace{\begin{pmatrix} 2 \\ 0 \\ 0 \end{pmatrix}}_{\alpha_5}, \underbrace{\begin{pmatrix} 0 \\ 2 \\ 0 \end{pmatrix}}_{\alpha_6}, \underbrace{\begin{pmatrix} 0 \\ 0 \\ 2 \end{pmatrix}}_{\alpha_7}.$$

So in this case it is  $m = 7$ . Inserting these multi-indices leads to the conditions presented above for each dimension.

As presented in [NÜ18], one can also include mixed moments, i.e. include multi-indices  $\alpha$  with non-diagonal entries and  $|\alpha| \leq N_m$ . For the monopolar Venant approach with mixed moments, the following vectors are added to the set of multi-indices:

$$\underbrace{\begin{pmatrix} 1 \\ 1 \\ 0 \end{pmatrix}}_{\alpha_8}, \underbrace{\begin{pmatrix} 1 \\ 0 \\ 1 \end{pmatrix}}_{\alpha_9}, \underbrace{\begin{pmatrix} 0 \\ 1 \\ 1 \end{pmatrix}}_{\alpha_{10}}.$$

Therefore it is  $m = 10$  here. Thus the problem to find the monopole strengths can be written as

$$\vec{t} = V \cdot \vec{q}.$$

This equation differs from equation (3.8) only in the matrix  $V$ , so we have to take the same steps to compute  $\vec{q}$ . We are going to use the same regularization matrix and parameters for all three approaches. Also we use the same way of applying the scaling factor  $a^{ref}$  to the monopolar approaches as we previously did for the multipolar Venant approach. The functionals

$$F_\lambda(\vec{q}) = \|\vec{t} - V \cdot \vec{q}\|_2^2 + \lambda \|W \cdot \vec{q}\|_2^2,$$

that we have to solve for all approaches will only differ in the matrix  $V$ .

In chapter 5 we are going to perform some tests with the three Venant approaches and compare them.

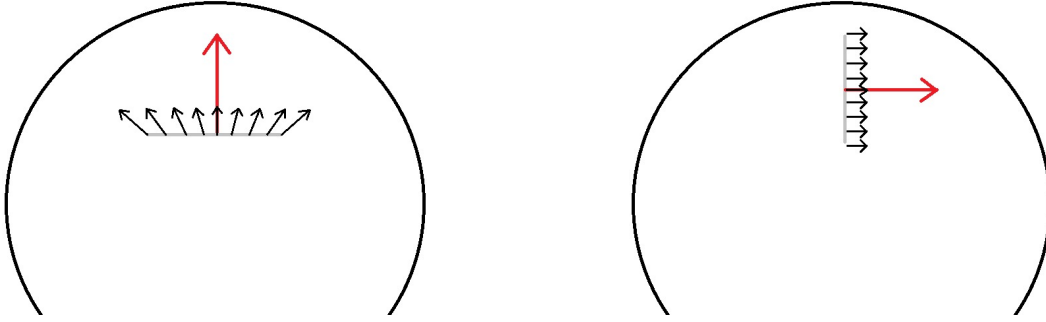


Figure 4.1: Illustration of a radial (left) and a tangential (right) patch. The red arrow represents the original dipole and the black arrows the patch dipoles. The illustration has been created by Jan Hüwel.

## 4 Quadrupolar Moments

As mentioned before, the mathematical dipole is often used to model brain activity, but it can only indirectly represent the extent of a source. To invest in multipoles with quadrupolar moments unequal zero, could be a way to improve the source reconstruction. The source extent underlying the EEG signal has been estimated to values of up to  $600 \text{ mm}^2$  [NU+00] and therefore should not be neglected. We will try to improve the representation of an extended source with using quadrupolar moments. There are already some studies where the contribution of multipolar sources to source analysis has been examined, see e.g. [BE18], [JE+02], [JE+04].

Looking back on equation (3.8), we see that the moments of the quadrupolar terms have been set to zero. In the following we are going to define some extended sources, *patches*, and see if we can improve the numerical forward solution to this scenario by setting the quadrupolar moments unequal zero.

At first we will define the patches we are going to compute the analytical solution with. We will only consider a spherical head model to ensure a controllable scenario and have a well defined goal function. The definition of the patches has been developed in collaboration with Jan Hüwel [HÜ21]. Each patch will be constructed from a single dipole by distributing a grid of patch dipoles around its position. Let  $M$  be the original dipole moment and  $R_1$  a normalized vector that is orthogonal to  $M$ . Let  $R_2$  be the cross product of  $M$  and  $R_1$  and therefore orthogonal to both of them. We will differentiate between *radial patches* and *tangential patches* for the original dipole being radial or tangential, respectively. The dipoles that are forming the patch, *patch dipoles*, are always going to have the same orientation as the original dipole and are scaled to have in sum the same moment strength as the original dipole. For radial dipoles, the patch dipoles moments are achieved by scaling the distance vector between the center of the sphere and the patch dipole's position, in order to ensure completely radial direction. For tangential dipoles, the patch dipoles are just going to have a scaled version of the original moment and do not need to be reoriented. For imagination of such patches see figure 4.1.

Now we will define the patches.

**Definition 4.1** (Radial Patches). *Let  $R_1$  and  $R_2$  be the orthogonal vectors described above. Let  $c \in \mathbb{R}^3$  be the center of a sphere,  $h \in \mathbb{R}$  a grid width and  $n \in \mathbb{N}_0$  the patch size such that  $N := (2n + 1)^2$  is the desired amount of patch dipoles. Given a radial dipole  $d_0 = (x_0, m_0)$  at position  $x_0 \in \mathbb{R}^3$  with moment  $m_0 \in \mathbb{R}^3$  such that  $\|m_0\| = 1$ , we define a radial patch*

around  $d_0$  as follows:

$$P_{rad} = \left\{ p_{ij} = (x_{ij}, m_{ij}) \in \mathbb{R}^3 \times \mathbb{R}^3 : i, j \in [-n, n] \cap \mathbb{Z}, \right. \\ \left. \begin{aligned} x_{ij} &= x_0 + ihR_1 + jhR_2, \\ m_{ij} &= \frac{1}{N} \frac{x_{ij} - c}{\|x_0 - c\|} \end{aligned} \right\} \quad (4.1)$$

**Theorem 4.2.** *A radial patch  $P_{rad}$  constructed from a radial dipole  $d_0$  fulfills:*

1.  $x_0 = \frac{1}{N} \sum_{i,j=-n}^n x_{ij}$
2.  $m_0 = \sum_{i,j=-n}^n m_{ij}$
3.  $m_{ij}$  is radial for all  $i, j \in [-n, n] \cap \mathbb{Z}$

Condition 1 indicates, that  $x_0$ , the original dipole's position, is the center of the patch and condition 2 that the sum of all patch dipole moments forms the original dipole moment. Let us proof this theorem.

*Proof.* 1.

$$\begin{aligned} \frac{1}{N} \sum_{i,j=-n}^n x_{ij} &= \frac{1}{N} \sum_{i,j=-n}^n (x_0 + ihR_1 + jhR_2) \\ &= \frac{1}{N} \sum_{i,j=-n}^n x_0 \\ &= \frac{N}{N} x_0 \\ &= x_0 \end{aligned}$$

2.

$$\begin{aligned} \sum_{i,j=-n}^n m_{ij} &= \sum_{i,j=-n}^n \frac{1}{N} \frac{x_{ij} - c}{\|x_0 - c\|} \\ &= \frac{1}{N} \frac{1}{\|x_0 - c\|} \left( \sum_{i,j=-n}^n x_{ij} - \sum_{i,j=-n}^n c \right) \\ &\stackrel{1}{=} \frac{1}{N} \frac{1}{\|x_0 - c\|} N(x_0 - c) \\ &= \frac{x_0 - c}{\|x_0 - c\|} \\ &\stackrel{*}{=} m_0, \end{aligned}$$

\* is valid because  $m_0$  is radial and scaled to norm 1, so it has to be equal.

3. Since  $m_{ij}$  is a scaled version of  $x_{ij} - c$ , it is trivially radial. □

**Comment 4.3.** *The radial patch can also be constructed for radial dipole moments  $m_0 \in \mathbb{R}^3$  with  $\|m_0\| \neq 1$ . Then the patch dipole moments  $m_{ij}$  just have to be multiplied by  $\|m_0\|$ . However, in our tests we will only consider dipole moments scaled to norm one.*

We will now take a look at patches for tangential dipoles in the same way.

**Definition 4.4** (Tangential Patches). *Let  $R_1$  and  $R_2$  be the orthogonal vectors described above. Let  $c \in \mathbb{R}^3$  be the center of a sphere,  $h \in \mathbb{R}$  a grid width and  $n \in \mathbb{N}_0$  the patch size such that  $N := (2n + 1)^2$  is the desired amount of patch dipoles. Given a tangential dipole  $d_0 = (x_0, m_0)$  at position  $x_0 \in \mathbb{R}^3$  with moment  $m_0 \in \mathbb{R}^3$ , we define a tangential patch around  $d_0$  as follows:*

$$P_{tan} = \left\{ \begin{aligned} p_{ij} &= (x_{ij}, m_{ij}) \in \mathbb{R}^3 \times \mathbb{R}^3 : i, j \in [-n, n] \cap \mathbb{Z}, \\ x_{ij} &= x_0 + ihR_1 + jhR_2, \\ m_{ij} &= \frac{1}{N}m_0 \end{aligned} \right\} \quad (4.2)$$

**Theorem 4.5.** *A tangential patch  $P_{tan}$  constructed from a tangential dipole  $d_0$  fulfills:*

1.  $x_0 = \frac{1}{N} \sum_{i,j=-n}^n x_{ij}$
2.  $m_0 = \sum_{i,j=-n}^n m_{ij}$
3.  $m_{ij}$  is tangential for all  $i, j \in [-n, n] \cap \mathbb{Z}$

*Proof.* 1. Identical to the proof of theorem 4.2.

2.

$$\sum_{i,j=-n}^n m_{ij} = \sum_{i,j=-n}^n \frac{1}{N}m_0 = m_0.$$

3. In order to prove this, we will show that  $m_{ij}$  is orthogonal to  $x_{ij} - c$  for all  $i, j \in [-n, n] \cap \mathbb{Z}$

$$\begin{aligned} \langle m_{ij}, x_{ij} - c \rangle &= \left\langle \frac{1}{N}m_0, x_0 + ihR_1 + jhR_2 - c \right\rangle \\ &= \frac{1}{N} \left( \langle m_0, x_0 - c \rangle + ih \langle m_0, R_1 \rangle + jh \langle m_0, R_2 \rangle \right) \\ &\stackrel{*}{=} 0, \end{aligned}$$

\* is valid because as  $m_0$  is tangential, it is orthogonal to  $x_0 - c$  and  $R_1, R_2$  were defined to be orthogonal to  $m_0$ . □

For these patches, we are going to compute an analytical solution, which is possible since we are only looking at spherical head models in this thesis. This analytical solution will be our goal function and we are going to try to approximate it with the multipolar Venant approach. Therefore we will compute the forward solution using the original dipole and, with the intention of better approximating the extend of the patch, give the quadrupolar moments a value.

One approach to give the quadrupole moments a value will be to compute them in the following way. The idea has been shown in [BE18] and is based on a series expansion using a Taylor series.

**Definition 4.6** (Computing of Quadrupole Moments). *Given a patch  $P$  of  $N \in \mathbb{N}$  dipoles  $(x_i, m_i) \in \mathbb{R}^3 \times \mathbb{R}^3, i = 1, \dots, N$  around dipole  $d_0 = (x_0, m_0)$ , we define the quadrupolar moments  $m_{quad} \in \mathbb{R}^{3 \times 3}$  of that patch as*

$$m_{quad} = \frac{1}{2} \sum_{i=1}^N \left( (x_i - x_0)m'_i + m_i(x_i - x_0)' \right).$$

With equation (3.8) in mind, we are going to replace the vector  $\vec{t}$  by

$$\begin{pmatrix} 0 \\ \bar{m}_1 \\ \bar{m}_2 \\ \bar{m}_3 \\ \bar{m}_{quad}[1, 1] \\ \bar{m}_{quad}[2, 2] \\ \bar{m}_{quad}[3, 3] \\ \bar{m}_{quad}[1, 2] \\ \bar{m}_{quad}[2, 3] \\ \bar{m}_{quad}[1, 3] \end{pmatrix},$$

with  $\bar{m}_{quad}[i, j] := \frac{m_{quad}[i, j]}{a^{ref}}$ . Unfortunately this way of computing the quadrupole moments leads to zero for all quadrupolar moments when using our tangential patches. As our tangential patches are highly regular and all patch dipoles have the same moment, they cancel each other. So we are only going to use this equation for radial dipoles. If a patch is not as regular as ours, which is likely to be the case for realistic patches, the equation could also be used for tangential dipoles.

As an alternative we will use an optimization to set the quadrupole moments. In chapter 5 we will describe the procedure in more detail.

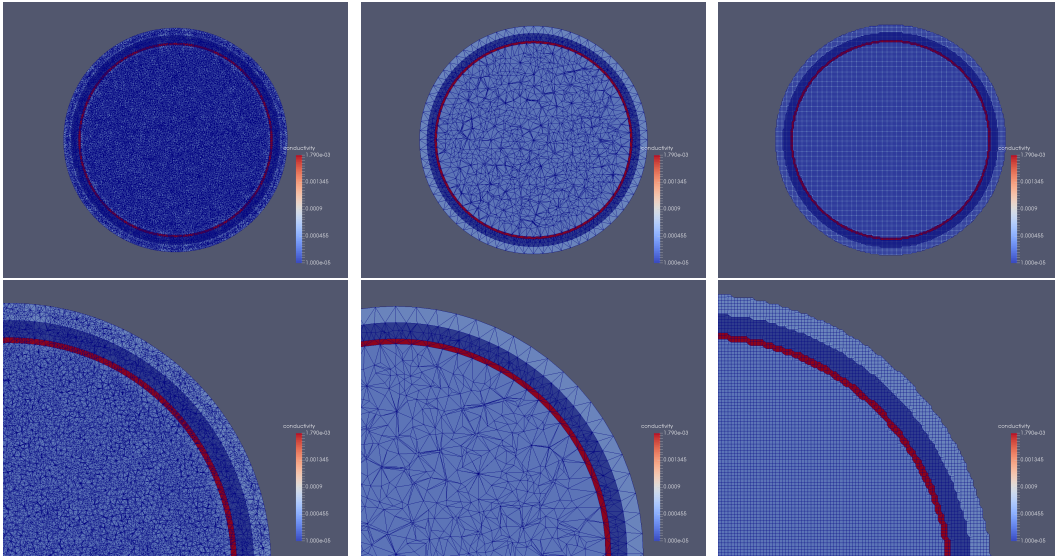


Figure 5.1: tet\_high

Figure 5.2: tet\_low

Figure 5.3: hex

## 5 Numerical Experiments

### 5.1 Multi-layer Sphere Setups for Evaluation Studies

In this chapter we want to perform some tests using the multipolar Venant approach. At first we will look at some parameters and find out which are the best to choose. Then we will look at how the multipolar Venant approach performs in comparison to the commonly used monopolar Venant. As a last experiment we will have a look at multipoles and the question of whether we can improve the approximation of an extended source by adding quadrupole moments to the multipolar Venant approach.

All tests are performed in a four-layer sphere model. Ideally, we would choose a realistic head model and compare the results to a reference solution, but there are no realistic models with a known reference solution. Therefore we choose a simplified 3D model, a series of concentrically nested spheres. For this kind of source model we can compute pointwise an analytical solution with a series expansion. This was derived by de Munck and Peters [DM+93]. So the setting is well controlled and we easily get a reference solution to compare our results with. We will use FieldTrip-SimBio (<http://fieldtriptoolbox.org>, [VO+18]) to compute the analytical solution. The source model distinguishes the conductive compartments brain, cerebrospinal fluid (CSF), skull and skin. We will use two tetrahedral meshes with different resolutions and one hexahedral mesh. See figures 5.1 - 5.3 for a visualization of the meshes.

The high resolutional tetrahedral model (tet\_high) was generated using TetGen (<http://wias-berlin.de/software/tetgen/>) by [VO+19] with a quality constraint (qc) and a volume constraint (vc). The quality constraint was set to 1.0. It determines the maximum of the ratio between the circumscribed ball and the shortest edge of a tetrahedron. A low value enforces the construction of well-shaped tetrahedra. The volume constraint is set to 1.12, it limits the maximal volume of each tetrahedron to 1.12 mm<sup>3</sup> and therefore enforces a uniformly high mesh resolution.

The tetrahedral mesh with lower resolution, tet\_low, has been generated using gmsh (<https://gmsh.info>) by [SC+20].

The hexahedral model was generated using FieldTrip-SimBio by [VO+19]. Instead of using

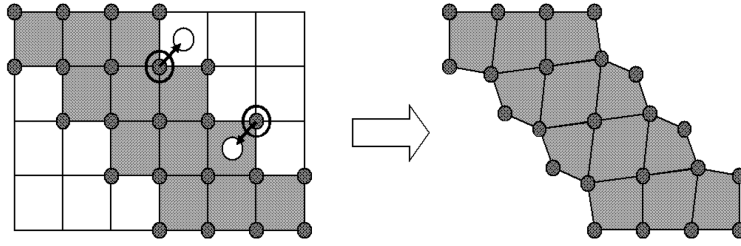


Figure 5.4: Concept of the hexahedral node-shift approach for the smoothing of interface boundaries in a 2D scenario: On the left side of the figure, the procedure is illustrated for only two boundary nodes, from one of which is moved outside and the other one is moved inside towards the centroids of their minority elements. The final result of the node-shift, a smoothed boundary representation using deformed hexahedra, is shown on the right side.[WO+07a]

a regular hexahedral mesh, we will use a geometry adapted one, where a node shift of 0.49 was applied [WO+07a]. This is the highest value that guarantees that all hexahedra remain convex [WO+07a]. In figure 5.4 the difference between a regular and a geometry adapted hexahedral mesh can be seen. Following [WO+07a], a geometry adapted mesh reduces both topography and magnitude error as it better adapts to the geometry of the sphere. In order to get a central overview of the models see table 5.1 and 5.2.

Table 5.1: Sphere Model

	Brain	CSF	Skull	Skin
Radius [mm]	78	80	86	92
Conductivity [S/m]	0.33	1.79	0.01	0.43

Table 5.2: Parameters of the Meshes

Mesh	Nodes	Elements	qc	vc [mm <sup>3</sup> ]	node shift
tet_high	801 633	4 985 234	1.0	1.12	-
tet_low	54 771	306 439	-	-	-
hex	3 342 701	3 262 312	-	-	0.49

As sources, we use a set of 19 000 dipoles at radii between 2 and 77 mm in 1 mm steps. For each source eccentricity there are dipoles at 125 random source positions with radial and tangential dipole orientation, respectively. All dipole moments are scaled to norm one. For some tests we will only use a subset of these dipoles. For evaluation we use the eccentricity of the source location, i.e. the quotient of the radius of the source position and the brain/CSF interface (78 mm) in percent. We will compare the error measure at different eccentricities. For the purpose of better readability, we rounded the eccentricities and compounded 250 dipoles to the same eccentricity in the plots. We evaluated the forward solution at 200 regularly distributed electrode positions on the surface of the sphere model.

As error measures, in order to see the difference between the analytical and the different numerical solutions, we use the RE (relative error), the RDM (relative difference measure)

and the MAG (magnitude error). They are defined as

$$\begin{aligned}
\text{RE}(u_{num}, u_{ana}) &= \|u_{num} - u_{ana}\|_2, \\
\text{RDM}(u_{num}, u_{ana}) &= \left\| \frac{u_{num}}{\|u_{num}\|_2} - \frac{u_{ana}}{\|u_{ana}\|_2} \right\|_2, \\
\text{MAG}(u_{num}, u_{ana}) &= \frac{\|u_{num}\|_2}{\|u_{ana}\|_2}.
\end{aligned} \tag{5.1}$$

Here  $u_{num} \in \mathbb{R}^s$ ,  $s \in \mathbb{N}$  the number of sensors, is the solution to the forward problem of the used numerical approximation and  $u_{ana} \in \mathbb{R}^s$  is the analytical solution which is used as a reference. For better visualization we will use the lnMAG instead of the MAG, which is the natural logarithm of the MAG. The RDM provides an approximation of the topography error and is bounded between 0 (no RDM error) and 2 (highest RDM error). The lnMAG indicates errors in potential magnitude, its optimal value is 0.

For the tests we use the software DUNEuro (DUNE for neurosciences). Thus the first step will be to introduce this software.

## 5.2 The Software DUNEuro

DUNEuro is an open source software toolbox for forward modeling in bioelectromagnetism. For a more detailed introduction see [SC+20]. The software is developed and used on Linux operating system. It can be downloaded from a Gitlab repository (<https://gitlab.dune-project.org/duneuro>), which is also linked from the webpage (<http://www.duneuro.org>). DUNEuro is based on the C++ software DUNE (distributed and unified numerics environment, <http://www.dune-project.org>) and has interfaces in Matlab (The Math Works Inc., Natick, Massachusetts, United States; <https://www.mathworks.com>) and Python (Python Software Foundation, <https://www.python.org>). There are already various approaches useable in DUNEuro and some more to follow, see [SC+20].

The monopolar Venant approach already existed in the software and the multipolar Venant has been implemented similar to the implementation of the approach in FieldTrip-SimBio, see [VO+18]. Many aspects like the choice of the monopole positions are the same for the monopolar and multipolar Venant. As seen before, it mainly differs in the matrix  $V$ .

In order to call the different approaches, we use the DUNEuro Matlab binding. We want to look at the different steps to call the multipolar Venant approach in the following. Additional information on this and other approaches can also be found in the wiki of the DUNEuro GitLab repository (<https://gitlab.dune-project.org/duneuro/duneuro/-/wikis>).

---

```
%% create driver object for tet_high
```

```
load(filename_grid)

cfg = [];
cfg.type = 'fitted';
cfg.solver_type = 'cg';
cfg.element_type = 'tetrahedron';
cfg.volume_conductor.grid.elements = uint64(mesh.tet-1)';
cfg.volume_conductor.grid.nodes = (mesh.pos)';
cfg.volume_conductor.tensors.labels = uint64(mesh.tissue-1);
cfg.volume_conductor.tensors.conductivities = ...
    [0.00033 0.00179 0.00001 0.00043];
driver = duneuro_meeeg(cfg);
```

At first a driver is created. The driver is a coarse grained interface for solving EEG and MEG forward problems. Different aspects are specified here. First, the general discretization type (`type`) is indicated, *fitted* implies that a mesh will be provided and standard CG- or DG-FEM can be used. The FEM-type (`solver_type`) *cg* says that we will use continuous galerkin methods. On top of that, the mesh and the corresponding conductivities are passed. With `element_type` we pass the element type of the mesh, which is either *tetrahedron* or *hexahedron*.

---

```
%% read electrodes
```

```
load(filename_electrodes);
electrodes = (elec.elecpos)';

cfg = [];
cfg.codims = '3';
cfg.type = 'closest_subentity_center';
driver.set_electrodes(electrodes, cfg);
```

As the next step the electrode positions are passed and projected to the mesh. The type `closest_subentity_center` specifies that the electrode positions are set to the closest subentity. The `codims` parameter represents the codimension of subentities to which the electrodes should be projected, 3 implies nodes.

---

```
%% compute transfer matrix
```

```
cfg = [];
cfg.solver.reduction = '1e-12';
transfer_matrix = driver.compute_eeg_transfer_matrix(cfg);
```

Then the transfer matrix can be computed (`driver.compute_eeg_transfer_matrix`). The transfer matrix provides a way to simplify the EEG forward problem. It arranges that the potential generated by a dipole is only computed at the sensor positions and not at all possible nodes of the mesh. Thus the computational costs are reduced greatly if the number of sensors is much smaller than the number of sources. The transfer matrix is the same for all forward approaches, therefore it can be computed before we even determine which approach to use.

---

```
%% read dipoles
```

```
load(filename_dipoles);
dipoles = [pos, dir]';
```

---

```
%% compute lead field matrix
```

```
cfg = [];
cfg.post_process = 'true';
cfg.subtract_mean = 'true';
cfg.source_model.type = 'multipolar_venant'; %'venant'
cfg.source_model.restrict = 'true'; %'false'
cfg.source_model.referenceLength = '20';
cfg.source_model.weightingExponent = '1';
cfg.source_model.relaxationFactor = '1e-6';
%cfg.source_model.mixedMoments = 'true'; %'false'
%cfg.source_model.numberOfMoments = '3';
%cfg.source_model.quadrupoles = [0,0,0,0,0,0];
cfg.source_model.initialization = 'closest_vertex';
lf = driver.apply_eeg_transfer(transfer_matrix, dipoles, cfg);
```

After reading the dipoles, which are passed as a  $n \times 6$  matrix containing the dipole locations and moments, the leadfield can be computed by `driver.apply_eeg_transfer_matrix`. Therefore the transfer matrix is multiplied by the right hand side. Before applying the transfer matrix, there are some parameters yet to be determined.

First of all, the source model (`source_model.type`). The multipolar Venant approach can be chosen by `multipolar_venant` and the monopolar venant is called `venant`. The meaning of the parameter `source_model.restrict` will get clear in the next section.

The `source_model.referenceLength` is the  $a^{ref}$  that we have seen before. We are going to set it to 20 mm in all our tests. The `source_model.weightingExponent` is our  $r$ , the exponent of the weighting matrix. Following [VO+19] and [HA19] we will set it to 1. The `source_model.relaxationFactor` is our  $\lambda$ . Following [HA19] a choice of  $10^{-6}$  leads to convincing results and therefore we are going to use this for all the following experiments. The

commented line `source_model.mixedMoments` is only needed if we set `source_model.type` to *venant* and it then determines if we use the monopolar Venant approach with or without mixed moments, *true* means that we use mixed moments.

Also the `source_model.numberOfMoments` is only needed in the monopolar case. We will set it to 3, which means that moments up to second order are considered. The parameter `source_model.initialization` determines how to choose the monopole locations. The method *closest\_vertex* uses the way we described earlier. It chooses the vertex closest to the source and its neighbors. The `source_model.quadrupoles` parameter we will use in our last experiments. There we will apply the multipolar Venant with quadrupole moments and with this parameter we can set the values.

The resulting leadfield then contains the potential at the electrodes for each dipole.

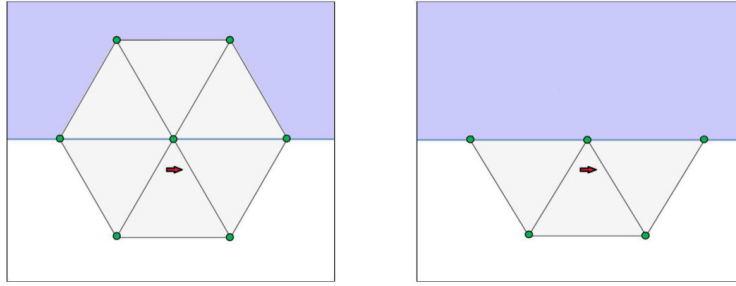


Figure 5.5: Used monopole locations, left: without restriction, right: with restriction [KR19]

### 5.3 Venants Condition for the Multipolar Venant Approach

In this section we will have a closer look at the parameter `source_model.restrict`. This is a bool parameter. Setting it to true means that for the monopole locations only those nodes that are in the same conductivity domain as the dipole are considered. See figure 5.5 to get an idea on how restriction works. The idea of cutting the monopole locations which lie outside the brain has been introduced by [ME15] and was called the *Venants Condition*. It says that for dipoles lying close to a conductivity jump it is possible that there are neighboring vertices lying in the next compartment. While choosing the monopole location it may happen that the monopoles are placed outside the brain and this may lead to errors in the numerical solution. Therefore it might be better to not take the monopoles outside the brain into account while computing the forward solution. On the other hand, as can be seen in figure 5.5, the cutting of the monopole locations in the next compartments leads to fewer monopole locations. The lack of enough monopoles may also lead to stronger numerical errors as there is a chance that the monopole locations are not uniformly distributed around the dipole location. Then the dipole potential cannot be represented accurately in all directions [HA19].

We want to check what consequences to restriction are shown using the multipolar Venant approach. For the monopolar Venant approach without mixed moments it has already been shown that the Venant Condition avoids high errors in high eccentricities [ME15]. The restriction is only relevant for the dipoles lying close to a conductivity jump, because dipoles lying deeper in the brain compartment will not have neighboring vertices in another compartment anyway. Therefore we will only look at the dipoles with the highest eccentricities.

In figure 5.6 you can see that for the `tet_high` mesh there are much more outliers if we do not use the restriction. Especially the RDM for tangential dipoles and the `lnMAG` for both radial and tangential dipoles show significant differences. The RDM for radial dipoles seems not to be that sensitive for restriction in this scenario. We do, however, see an improvement in applying the Venants Condition, so we will use the restriction for this mesh in the following.

Figure 5.7 shows that there are no significant differences if we use our hex mesh, neither in RDM nor in `lnMAG`. As the Venants Condition has been applied in comparable studies like [HA19], [VO+19], we are going to use the restriction for this model, too.

For the `tet_low` mesh we did not only consider the values at the highest eccentricity but also at eccentricity 0.96. Due to the coarseness of the mesh, monopole locations outside the brain compartment seem to be considered even for dipoles at this eccentricity. In figure 5.8 we see differences between the restricted and the not restricted models at eccentricity 0.96. Unfortunately, it is rather unclear which approach performs better. For tangentially oriented

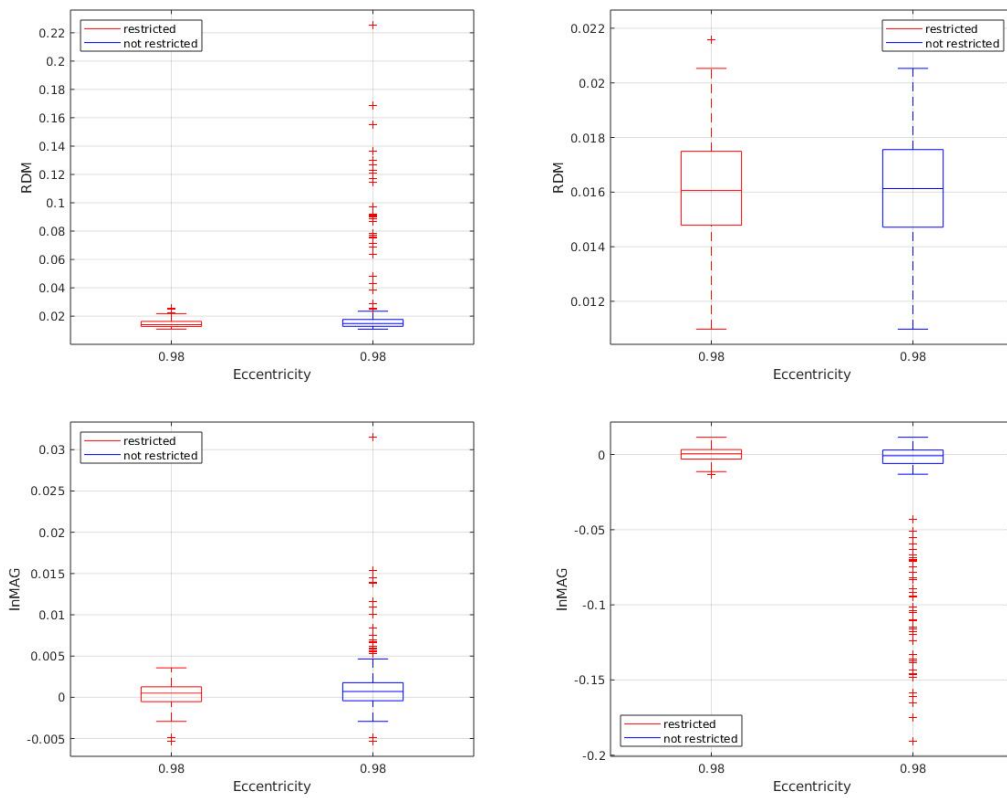


Figure 5.6: RDM (top row) and lnMAG (bottom row) for tangential (left column) and radial (right column) source orientations for model `tet_high`. Comparing the multipolar Venant approach with restriction (*restricted*) and without restriction (*not restricted*).

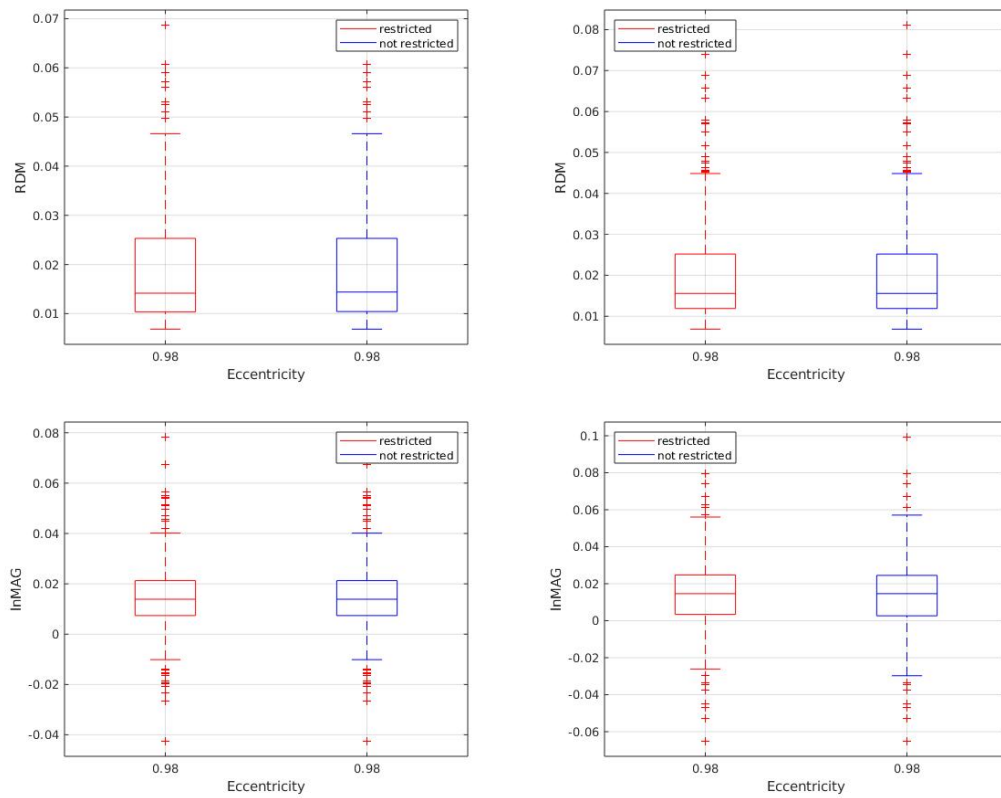


Figure 5.7: RDM (top row) and InMAG (bottom row) for tangential (left column) and radial (right column) source orientations for model hex. Comparing the multipolar Venant approach with restriction (*restricted*) and without restriction (*not restricted*).

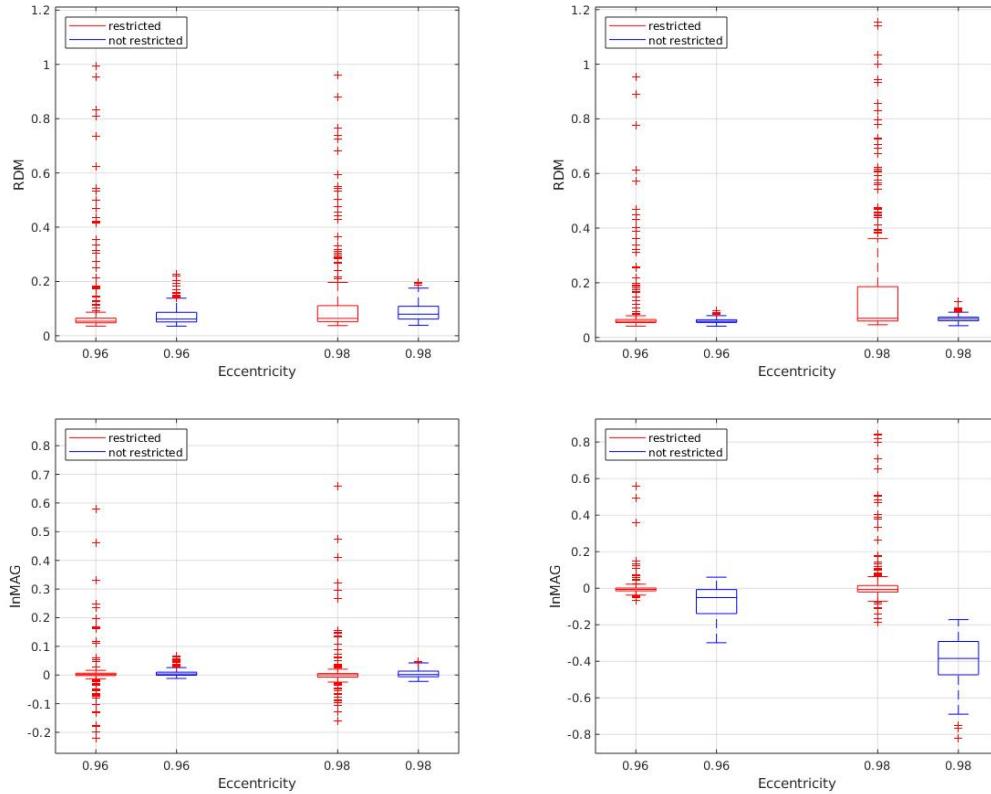


Figure 5.8: RDM (top row) and lnMAG (bottom row) for tangential (left column) and radial (right column) source orientations for model `tet_low`. Comparing the multipolar Venant approach with restriction (*restricted*) and without restriction (*not restricted*).

dipoles we observe more outliers in both RDM and lnMAG when looking at the restricted case. However, ignoring the outliers, at least the RDM at 0.96 shows a slightly better performance using the restricted model. For radial dipoles the lnMAG of the restricted model shows clearly better performance at both eccentricities. In contrast the RDM is better for the not restricted model, especially looking at eccentricity 0.98.

The non-optimal performance when using the Venant condition might result from our way of choosing the monopole locations. As the mesh is coarser, a dipole lying close to the conductivity jump has more neighboring vertices which lie in the next compartment and are therefore ignored when we use restriction. This may lead to a too small number of monopole locations. This problem might be solved by forcing the algorithm to take more vertices into account that are in the same compartment as the dipole, see [HA19].

As shown by [ME15] the restricted model to be better for the monopolar Venant approach, and as we want to ensure comparability between our different test scenarios, we are going to use the restricted model for the `tet_low` mesh, too.

As we see that the Venant Condition does not lead to convincing results in all scenarios, one could suggest another way to proceed with monopole locations outside the brain compartment. Instead of cutting them one could try to weight the monopoles lying in different compartments with the conductivity of the particular compartment. This way the inaccuracy observed when not using restriction might also be reduced and there would always be enough monopole locations. This might be a future area of investigation.

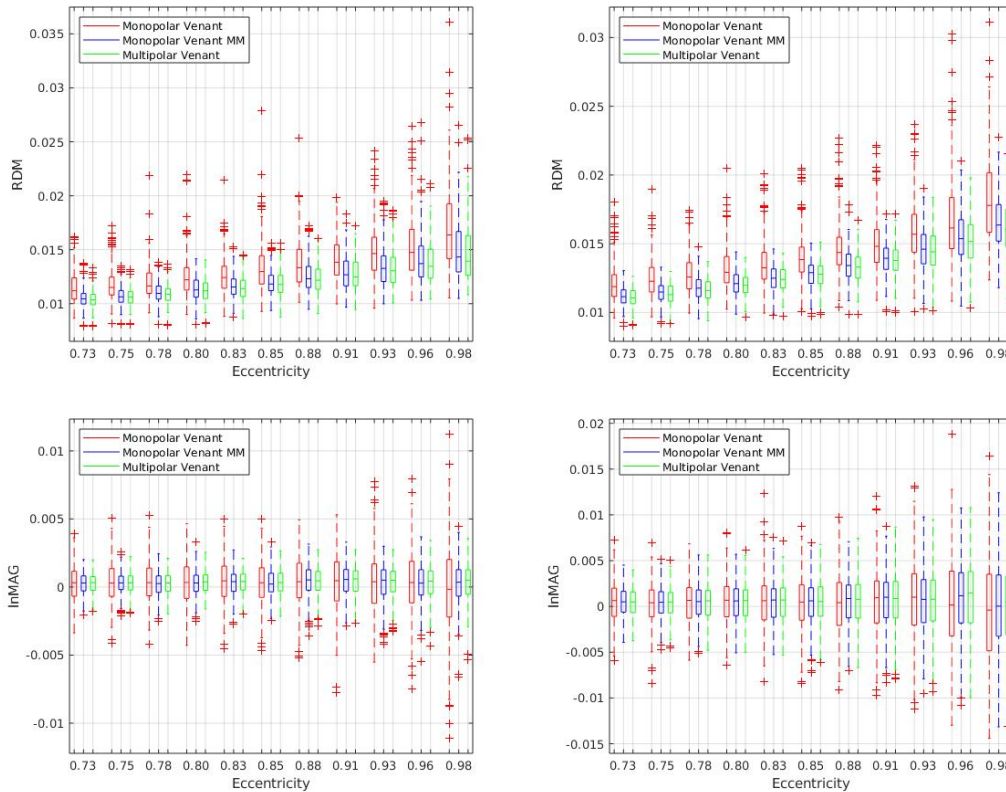


Figure 5.9: RDM (top row) and lnMAG (bottom row) for tangential (left column) and radial (right column) source orientations for model `tet_high`. Comparing the monopolar Venant approach without mixed moments (*Monopolar Venant*), the monopolar Venant approach with mixed moments (*Monopolar Venant MM*) and the multipolar Venant approach (*Multipolar Venant*).

## 5.4 Comparison of Multipolar and Monopolar Venant Approaches

Now, having set all parameters, we are able to compare the multipolar Venant approach to the commonly used monopolar Venant approach. As outlined before, we can consider the monopolar Venant approach with and without mixed moments. The comparison between the multipolar Venant approach and the monopolar Venant approach with mixed moments has not yet been carried out before. For the monopolar Venant approaches we use the same parameters as for the multipolar Venant.

In figure 5.9 we see the results for the high resolution tetrahedral mesh. As a first result we notice that the monopolar Venant approach with mixed moments shows better performance in both RDM and lnMAG for tangential and radial dipoles than the monopolar Venant approach without mixed moments. This fits to the findings of [NÜ18]. Nevertheless, the multipolar Venant approach outperforms both of them and shows even slightly better results than the monopolar Venant approach with mixed moments for all modalities.

All approaches show an error rise when looking at the highest eccentricities, but the multipolar Venant approach presents the lowest values. High eccentricities are of special interest. In realistic scenarios the source of brain activity normally is close to the head surface, in the gray matter compartment, and thus is best represented by eccentric sources. Therefore a good performance is especially important for these dipole locations.

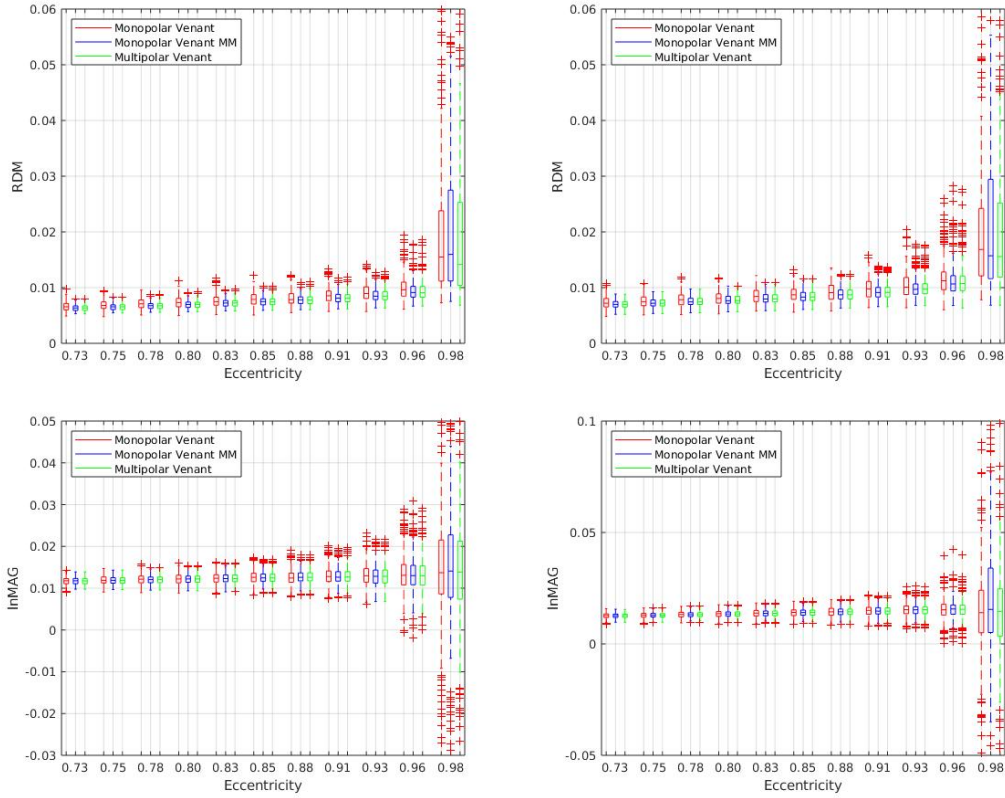


Figure 5.10: RDM (top row) and lnMAG (bottom row) for tangential (left column) and radial (right column) source orientations for model hex. Comparing the monopolar Venant approach without mixed moments (*Monopolar Venant*), the monopolar Venant approach with mixed moments (*Monopolar Venant MM*) and the multipolar Venant approach (*Multipolar Venant*).

In figure 5.10 the results for the hexahedral mesh can be seen. Here the differences between the approaches are less clear but still the multipolar Venant performs rather well in comparison to the monopolar Venant approaches. For the highest eccentricities the error measures for all approaches show a high rise. As said before, this could be reinforced by the restriction as it leads to fewer monopole locations and the fact that the hexahedral mesh cannot represent the sphere surfaces as well as the tetrahedral mesh. Nonetheless the multipolar approach seems to be less sensitive than the monopolar Venant approach with mixed moments, which, for the highest eccentricity, performs even worse than the monopolar Venant without mixed moments.

In figure 5.11 the results for the tet\_low mesh can be seen. As expected from our tests on the restriction, the multipolar Venant approach shows high errors in RDM for the highest eccentricities. Here it is outperformed by both monopolar Venant approaches. Especially the monopolar Venant approach with mixed moments does not seem to be very sensitive to fewer monopole locations, at least when looking at the RDM. As mentioned before, [HA19] presented another approach to choose the monopole locations. This could improve the multipolar Venant approach so that it may outperform the monopolar Venant approaches in a coarse grid scenario, too. Looking at less eccentric sources, the multipolar Venant approach again leads to the best results in RDM. For lnMAG, the multipolar Venant approach shows

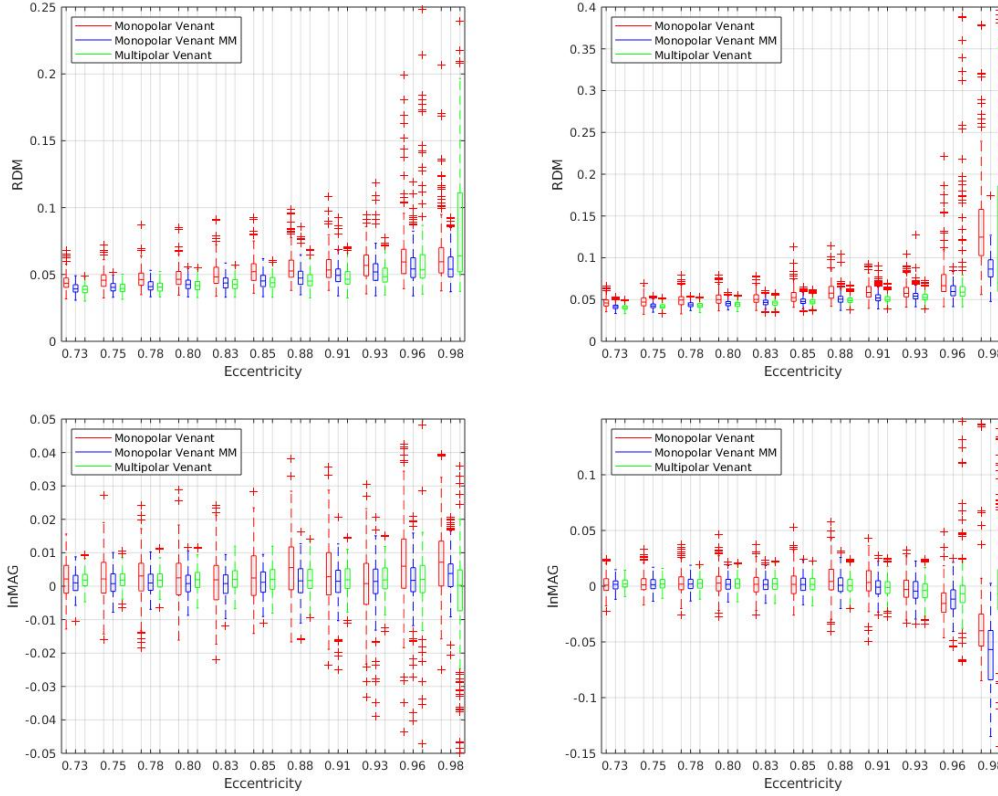


Figure 5.11: RDM (top row) and lnMAG (bottom row) for tangential (left column) and radial (right column) source orientations for model `tet_low`. Comparing the monopolar Venant approach without mixed moments (*Monopolar Venant*), the monopolar Venant approach with mixed moments (*Monopolar Venant MM*) and the multipolar Venant approach (*Multipolar Venant*).

the best performance, too. Here, especially at highest eccentricity for radial dipoles its error is on a much lower grade than the error measure for the monopolar approaches.

All in all, comparing the results for the `tet_high` mesh in figure 5.9 and for the `tet_low` mesh in figure 5.11, we can see that especially at high eccentricities the overall performance of the approaches is much better for the higher resolution mesh. This indicates the importance of investing in a high resolution model when trying to compute exact forward solutions. Resulting from the way of choosing the monopole locations as the neighboring vertices, for the Venant approaches the number of FE nodes between the dipole and the conductivity jump may determine the accuracy of the forward solution even more than the spatial distance. Therefore the coarse grid leads to much higher numerical errors than the finer one.

Taking all test scenarios into account, the high and low resolution tetrahedral mesh and the hexahedral mesh, the multipolar Venant approach shows a very good performance in comparison to the known monopolar Venant approaches. For the high resolution tetrahedral mesh it clearly outperforms the monopolar Venant approaches. The monopolar Venant approach without mixed moments has been tested in many studies like [BA+15] or [LE+09] and has always shown a performance superior to that of other approaches based on the classical continuous Galerkin (CG)-FEM. In [NÜ18] has been shown that the monopolar Venant approach with mixed moments performs even better in tetrahedral meshes. From our results we can deduce that the multipolar Venant approach outperforms both of them

and therefore most other approaches based on CG-FEM as well. For the hexahedral mesh the differences were less clear and for high eccentricities all approaches show a high error rise. This could be result of the fact that the hexahedral mesh cannot represent the sphere surfaces as well as the tetrahedral mesh. Anyway, the multipolar Venant approach shows slightly better performance than the monopolar Venant approach with mixed moments when looking at the highest eccentricities. For lower eccentricities there are no striking differences between the approaches, but the multipolar Venant approach performs marginally better than the monopolar approaches. Therefore the multipolar Venant approach seems to be a good approach for hexahedral meshes, too. The only apparent weakness of the multipolar Venant approach seems to occur when looking at coarse meshes and taking too few monopole locations into account. There, for high eccentricities, in RDM error the multipolar Venant approach is outperformed by both monopolar Venant approaches. As mentioned before, [HA19] suggested to solve this problem by changing the process of choosing the monopole locations. This should be a future goal to integrate in DUNEuro, too. It should be possible for the user to define a minimal number of monopole locations which the algorithm should then find in the brain compartment. Chances are good that the multipolar Venant then shows good results for coarse grids, too. On top of that in realistic tests, one should always try to create a grid fine enough to ensure that all neighboring vertices of a possible source position are within the brain compartment. That way the weakness of the multipolar Venant approach actually should not occur in realistic tests anyway. And, however, for less eccentric sources the multipolar Venant approach still shows the best performance.

Table 5.3: Patches

Patch Size $n$	Number of Dipoles	Patch Extent [mm <sup>2</sup> ]
4	81	16
14	841	196
24	2401	576

## 5.5 Approximation of Extended Sources

In the following experiments we will consider sources not as point sources but as patches of activity. We will use patches as defined in chapter 4. For the first tests, as *original dipoles* around which we build the patches, we use three sets of ten dipoles, respectively. One set at eccentricity 0.72, one at 0.82 and one at eccentricity 0.9. We do not use dipoles at higher eccentricities to ensure that even for larger patches all patch dipoles lie in the brain compartment of the source model. Also, for the most eccentric dipoles we do not use the largest patch scenario as there were patch dipoles lying outside the brain compartment, too. For each dipole of a set we construct a patch around it and compute the analytical solution for all of the patch dipoles. Then we sum up the analytical solutions for all patch dipoles of one patch. This represents the potential at the EEG sensor positions for all patch dipoles of one patch being activated at the same time and will be our goal function to compare the multipolar Venant approach to. This, of course, is not a completely realistic scenario, either. An extended source activity in the brain might be more smooth and not just at some points in the activated area. However, it is a way to get a first idea of the impact of quadrupole moments. As we know from the principle of Saint Venant, the potential measured at the EEG sensor positions should be similar for some activated points which lie close to each other and an uniformly distributed activity in the same area.

The parameters for the multipolar Venant approach remain the same as in the last sections. For our studies we use a grid width  $h = 0.5$  mm and investigate different patch sizes  $n$  which lead to different numbers of dipoles and different extents of the patch. See table 5.3 for detailed information.

As a first experiment we want to see for both radial and tangential patches how much the performance of the multipolar Venant approach in representing a patch can be improved by using quadrupolar moments. Therefore we use a non-linear least squares optimization over the relative error between the analytical solution and the forward solution with the quadrupole moments as variables. We made use of the Matlab function *lsqnonlin*, as the lower bound we set -1 for all quadrupole moments and as the upper bound 1. For radially oriented dipoles we will also look at the performance of computed quadrupoles as defined in definition 4.6.

In order to get an idea of the impact of quadrupoles on different meshes, eccentricities, dipole orientations and patch sizes, we can look at the norm of the quadrupole moments. Therefore we computed the  $L_2$ -norm of the optimized quadrupole moments for every dipole of an original-dipoles-set and then took the mean of these values for each set. See table 5.4 for an insight into the results. A higher value represents quadrupoles with larger entries and therefore the quadrupoles have a greater impact than in scenarios with smaller values.

Let us at first look at tangential dipoles and patches. In figure 5.12 the RDM und lnMAG measures for the different scenarios using the tet\_high mesh can be seen. For all eccentricities, we observe that the error rises with rising patch size. Looking at the RDM, we also see that the improvement of using quadrupole moments increases with increasing patch size. This fits to the values in table 5.4. There we find higher values for bigger patches.

Table 5.4:  $L_2$ -norm of the optimized quadrupolar moments for each dipole set.

Mesh	Eccentricity	Tangential			Radial		
		Patch Size			Patch Size		
		4	14	24	4	14	24
tet_high	0.72	0.05	0.05	0.08	0.07	0.12	0.28
	0.82	0.06	0.06	0.1	0.08	0.13	0.26
	0.9	0.06	0.07	-	0.08	0.13	-
tet_low	0.72	0.2	0.2	0.2	0.20	0.23	0.32
	0.82	0.21	0.21	0.2	0.25	0.29	0.39
	0.9	0.23	0.22	-	0.27	0.29	-
hex	0.72	0.12	0.1	0.06	0.14	0.22	0.36
	0.82	0.12	0.09	0.04	0.14	0.22	0.36
	0.9	0.11	0.07	-	0.14	0.22	-

The patches eccentricity seems to change the influence of the quadrupoles only a little, we observe slightly rising values with more eccentric patches. In lnMAG measure we find that the values for the dipole and the multipole diverge. While the dipole underestimates the magnitude more and more with rising patch size, the lnMAG values for the multipole rises with increasing patch size and overestimate the magnitude more and more. At some point the lnMAG is even worse for the multipole. This may result from our way of optimization. As we optimize over the relative error - which somehow represents both the RDM and the lnMAG - a value that strongly improves the RDM can worsen the lnMAG. Nonetheless, if we assume that a low RDM, as it represents the location and orientation of the source, is often more important in practice, we could interpret this result as a argument for using multipoles.

In figure 5.13 we see the results for tangential dipoles using the hex mesh. Here we find a trend that is contrary to that for the tet\_high mesh. While the RDM for the small patch is improved by the use of multipoles, for bigger patches it is even worse than the pure dipole. For the lnMAG we now see that both the dipole and the multipole overestimate the magnitude for all patch sizes and eccentricities. While the lnMAG for the dipole decreases and gets better for bigger patches, the lnMAG for the multipole rises for larger patches. However, the lnMAG using the multipole is better than the dipole for all test scenarios. Thus, in contrast to the last test here we see the improvement in lnMAG instead of RDM. In table 5.4 we also observe a contrary development in the norm of the quadrupole moments in comparison to the tet\_high mesh. The norm decreases with increasing patch size. This may explain the improvement of the lnMAG and worsening of the RDM in this case. Also the values get slightly smaller for more eccentric patches, so we see a trend contrary to the tet\_high mesh here, too.

As a last experiment for the tangential patches we want to look at the tet\_low mesh, figure 5.14. At first we observe that the differences between the different patch sizes do not have such a profound impact on the error measures in this case. For the dipole we can see the same trends in RDM in lnMAG as for the tet\_high mesh (figure 5.12), but much less clear. However, what is clear here is the improvement that comes with using the multipole. It shows better performance for all eccentricities in both RDM and lnMAG. Looking at table 5.4 we also observe, that the quadrupole moments hardly change between the different patch sizes, which fits to the rarely changing errormeasures. Only a slight rise with increasing eccentricity can be observed.

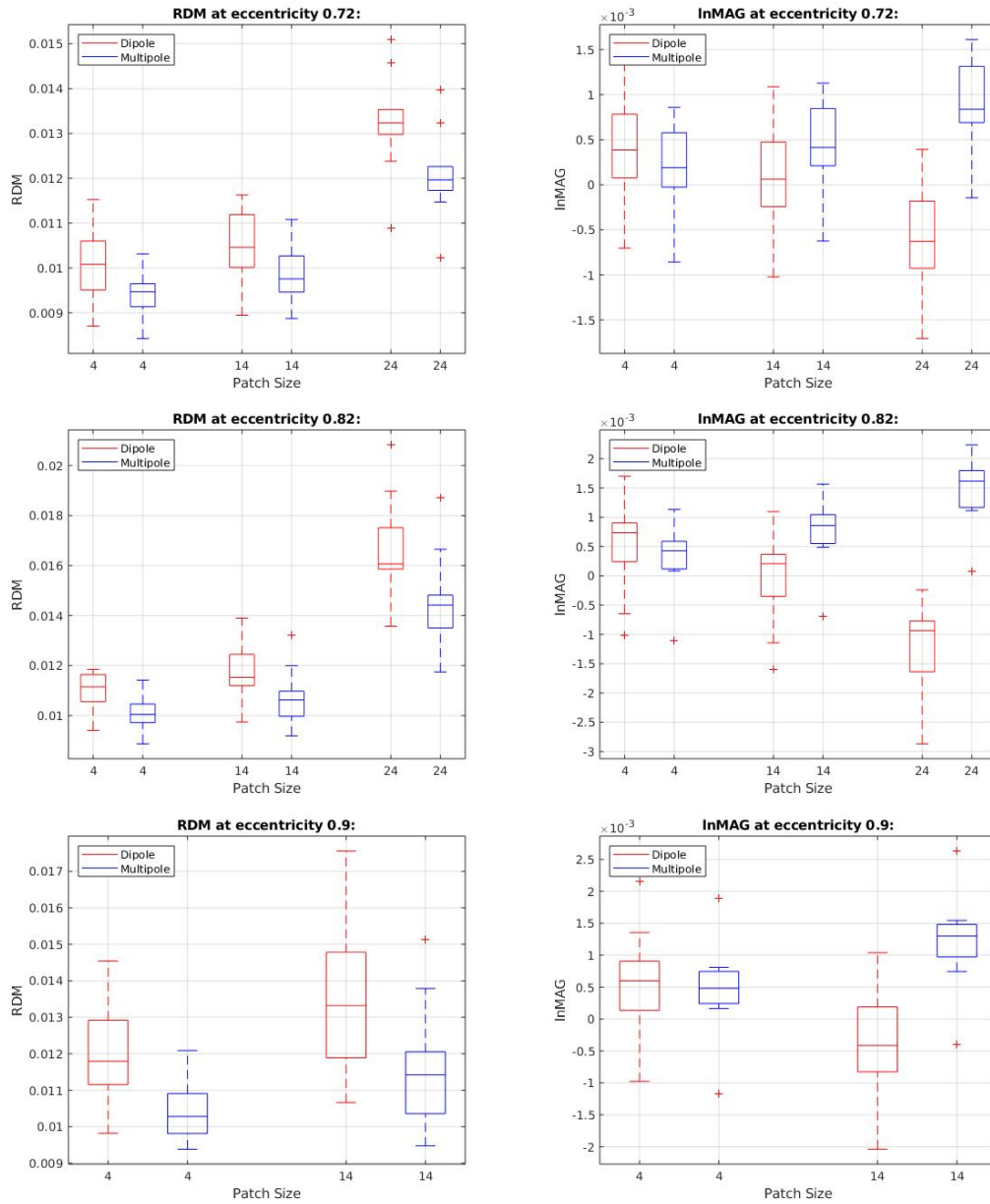


Figure 5.12: RDM (left column) and lnMAG (right column) for tangential patches at eccentricity 0.72 (top row), 0.82 (mid row) and 0.9 (bottom row) for model `tet_high`. Comparing the multipolar Venant approach using only dipolar moments (*Dipole*) and additional optimized quadrupolar moments (*Multipole*).

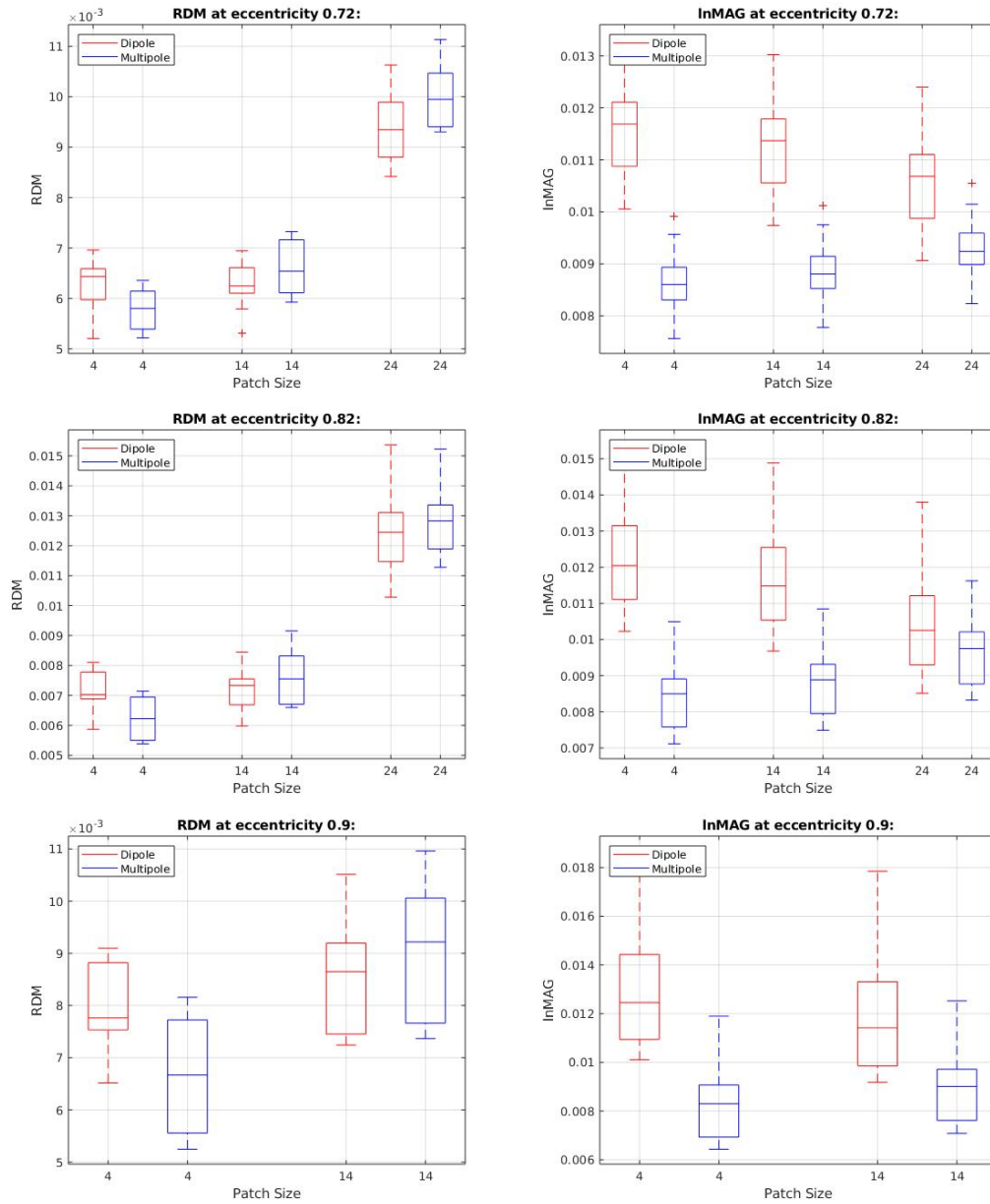


Figure 5.13: RDM (left column) and lnMAG (right column) for tangential patches at eccentricity 0.72 (top row), 0.82 (mid row) and 0.9 (bottom row) for model hex. Comparing the multipolar Venant approach using only dipolar moments (*Dipole*) and additional optimized quadrupolar moments (*Multipole*).

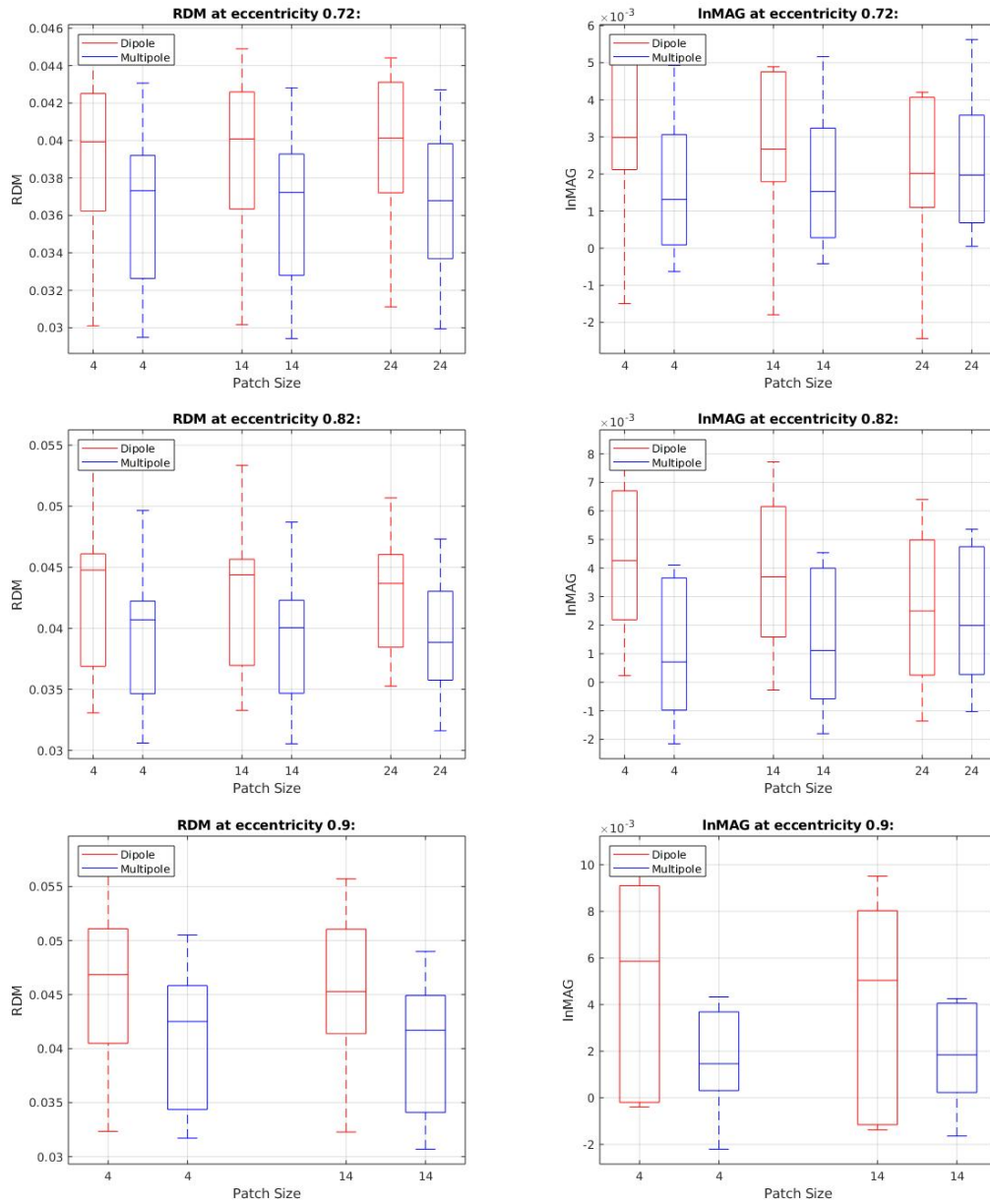


Figure 5.14: RDM (left column) and InMAG (right column) for tangential patches at eccentricity 0.72 (top row), 0.82 (mid row) and 0.9 (bottom row) for model `tet_low`. Comparing the multipolar Venant approach using only dipolar moments (*Dipole*) and additional optimized quadrupolar moments (*Multipole*).

Now we will look at the results for the same experiment using radial dipoles and patches. Additionally to the optimized quadrupolar moments, we will also consider computed quadrupolar moments as defined in definition 4.6.

Again, we will start with the `tet_high` mesh. At first we look at the RDM for the different scenarios, see figure 5.15. We observe that the use of multipoles with both computed and optimized quadrupolar moments improves the performance. The improvement gets stronger with increasing patch size. As expected, a small patch is already relatively well approximated by a pure dipole, but for bigger patches the need to consider the physical extend of the source gets more important. For the computed quadrupolar moments we also observe that the improvement increases with more eccentric sources. Especially for patch size 14 we see that at eccentricity 0.72 there is hardly any difference between the dipole and the multipole with computed quadrupoles, while at eccentricity 0.9 there is a clear difference. This may result from the fact that the error for the pure dipole increases for more eccentric patches and the error for the multipole approximately stays the same. As expected, when looking at the multipole with optimized quadrupoles we see that they show a better performance than the multipole with computed quadrupoles. Here, there already is an improvement in RDM for patch size 4 and the improvement increases with increasing patch size. Contrary to the computed quadrupoles, the improvement by the multipole with optimized quadrupoles hardly shows a difference between the different eccentricities. This fits to the values in table 5.4 where we see that the norm of the optimized quadrupolar moments stays approximately the same for the different eccentricities. Looking at the `lnMAG`, again we see that for patch size 4 there is nearly no difference between the pure dipole and the multipoles. For patch size 14 we observe that especially the computed quadrupoles improve the errors, even more than the optimized quadrupolar moments. For patch size 24 we also see an improvement that comes with using the multipole and here, again, the optimized quadrupolar moments show the best performance. All in all, we can deduce that using multipoles provides a strong improvement in the approximation of extended sources. The bigger the patch is the more quadrupolar moments are needed. The computed quadrupoles already show a good performance, but with the optimized values we see that even better results can be achieved at some points.

In figure 5.16 we see that for radial dipoles the results for the hexahedral mesh are similar to the result for the `tet_high` mesh. For RDM again we see that the use of quadrupolar moments reduces the errors and this improvement gets stronger with increasing patch size. For the hex mesh we already see a difference between the pure dipole and the multipole for patch size 4, but as it still is rather small, one can deduce that the pure dipole represents this patch size well enough. For patch size 14 we observe that the multipole with computed quadrupoles performs almost as well as the multipole with optimized quadrupoles. For patch size 24 the difference between the computed and optimized quadrupoles increases again, but still the multipole with computed quadrupoles strongly improves the RDM. Between the different eccentricities we do not see any difference this time, here the error of the pure dipole and the multipoles show an equal error rise with more eccentric patches. The multipole with optimized quadrupolar moments again has a growing impact for bigger patch sizes. This trend fits the findings of table 5.4, where we observe that the norm of the optimized quadrupolar moments rises with increasing patch size. Looking at the `lnMAG`, we see that the improvement that comes with using multipoles increases with rising patch size here, too. For patch size 4 the difference between the dipole and the multipole with computed quadrupolar moments is rather small, only the optimized quadrupoles show a stronger improvement. For patch size 14 we, again, observe that the computed quadrupoles show a strikingly good performance. Here the multipole with computed quadrupolar moments shows nearly the same error as for optimized quadrupolar moments, although the difference is slightly bigger with increasing eccentricity. For patch size 24 again the opti-

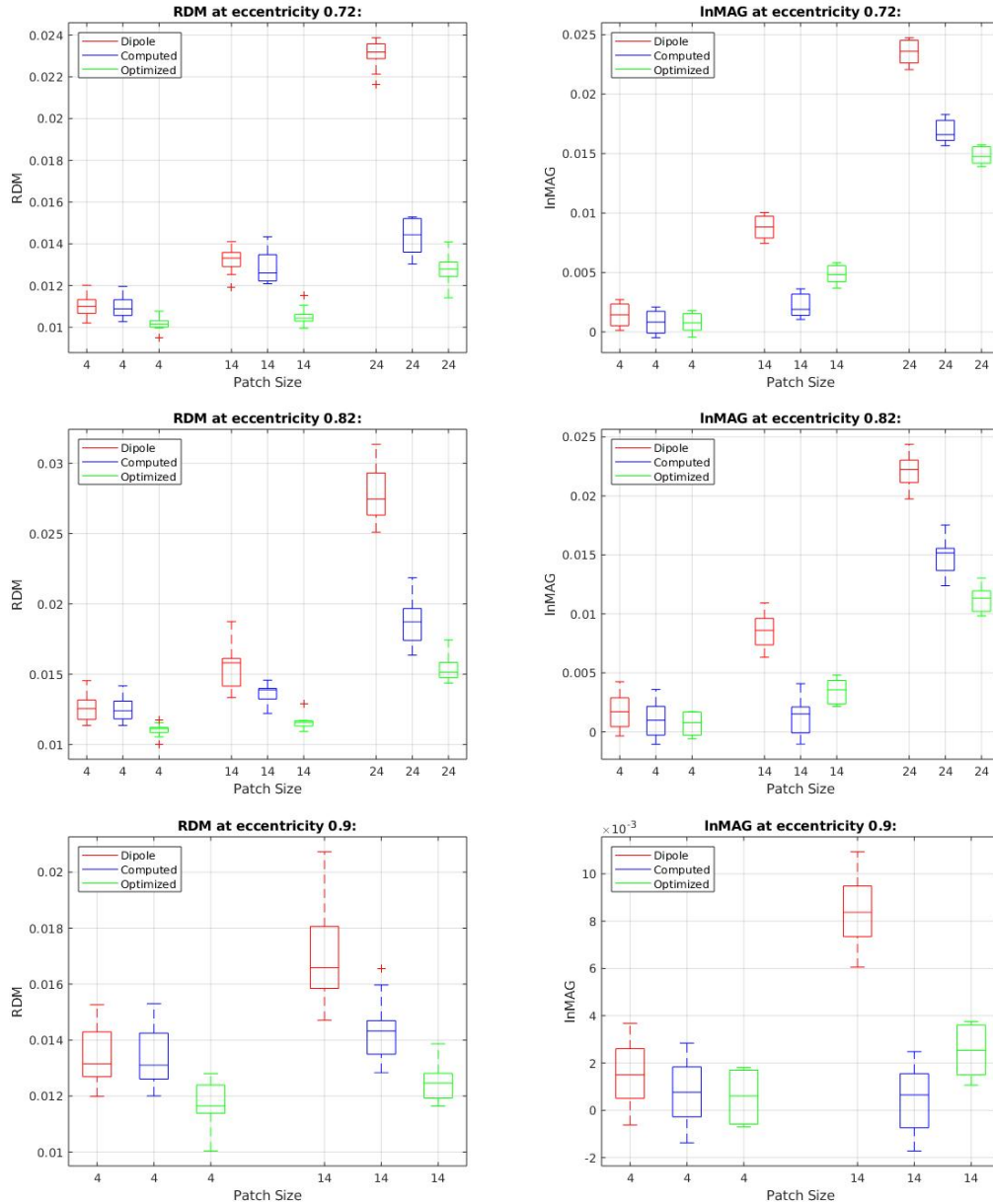


Figure 5.15: RDM (left column) and InMAG (right column) for radial patches at eccentricity 0.72 (top row), 0.82 (mid row) and 0.9 (bottom row) for model *tet\_high*. Comparing the multipolar Venant approach using only dipolar moments (*Dipole*), multipolar moments with computed quadrupolar moments (*Computed*) and multipolar moments optimized quadrupolar moments (*Optimized*).

mized quadrupolar moments show the lowest errors, but the computed ones improve the approximation of the magnitude in comparison to the pure dipole, too.

See figure 5.17 for the results using the `tet_low` mesh. At first we observe that the differences between the pure dipole approach and the multipolar approach are much less clear than for the `tet_high` and the hex mesh. This may result from the overall high errors for the coarse tetrahedral mesh. The improvement that comes with using multipoles therefore has a lower percentage than for the other meshes. Nonetheless, we can find the same trends. The multipole with computed quadrupolar moments improves the performance in both RDM and `lnMAG` in comparison to the pure dipole and this improvement gets stronger with increasing patch size. Also the multipole with optimized quadrupolar moments shows even lower errors, except for the `lnMAG` for patch size 14, where it is outperformed by the computed quadrupolar moments. As for the hex mesh, we do not see any markable change relating to the eccentricity of the patches. In contrast, in table 5.4 we see that the norm increases for more eccentric sources. This could result from the fact that the `tet_low` mesh generally shows high errors for eccentric sources. The optimization might compensate these modelling errors and therefore lead to higher values for more eccentric patches. The gain of impact with increasing patch size again fits to the values in table 5.4.

All in all, looking at the optimization for the quadrupole moments, we can observe that quadrupoles in fact have a strong impact when trying to represent patches of activity. For tangential dipoles we could not find a clear trend whether the error measures can be improved, as the multipole has shown worse performance than the pure dipole in some scenarios. This could be a result of our way of constructing the patch, which is very regular and therefore already well represented by a pure dipole.

However, for radial dipoles we see a clear improvement when using multipoles instead of pure dipoles for representing the patches. The introduced way of computing the quadrupolar moments has demonstrably brought an improvement in comparison to the pure dipole which gets stronger with increasing patch sizes. The optimized quadrupolar moments have shown that even stronger differences can be achieved regarding some aspects, so there might be an even better way to determine quadrupolar moments than the one defined in 4.6. As expected, we saw that the impact of the quadrupole moments increases with increasing patch size for the optimized quadrupolar moments, too, so for bigger patches stronger quadrupole moments are needed. Moreover we can deduce that optimal quadrupole moments seem to depend on the mesh and the patch size rather than on the eccentricity of the patch. In the following we will have a closer look at the optimized and computed quadrupolar moments for radial dipoles. We will try to visualize them in order to get a better understanding of how they should be shaped for optimal results, which might lead to an even better approach of computation.

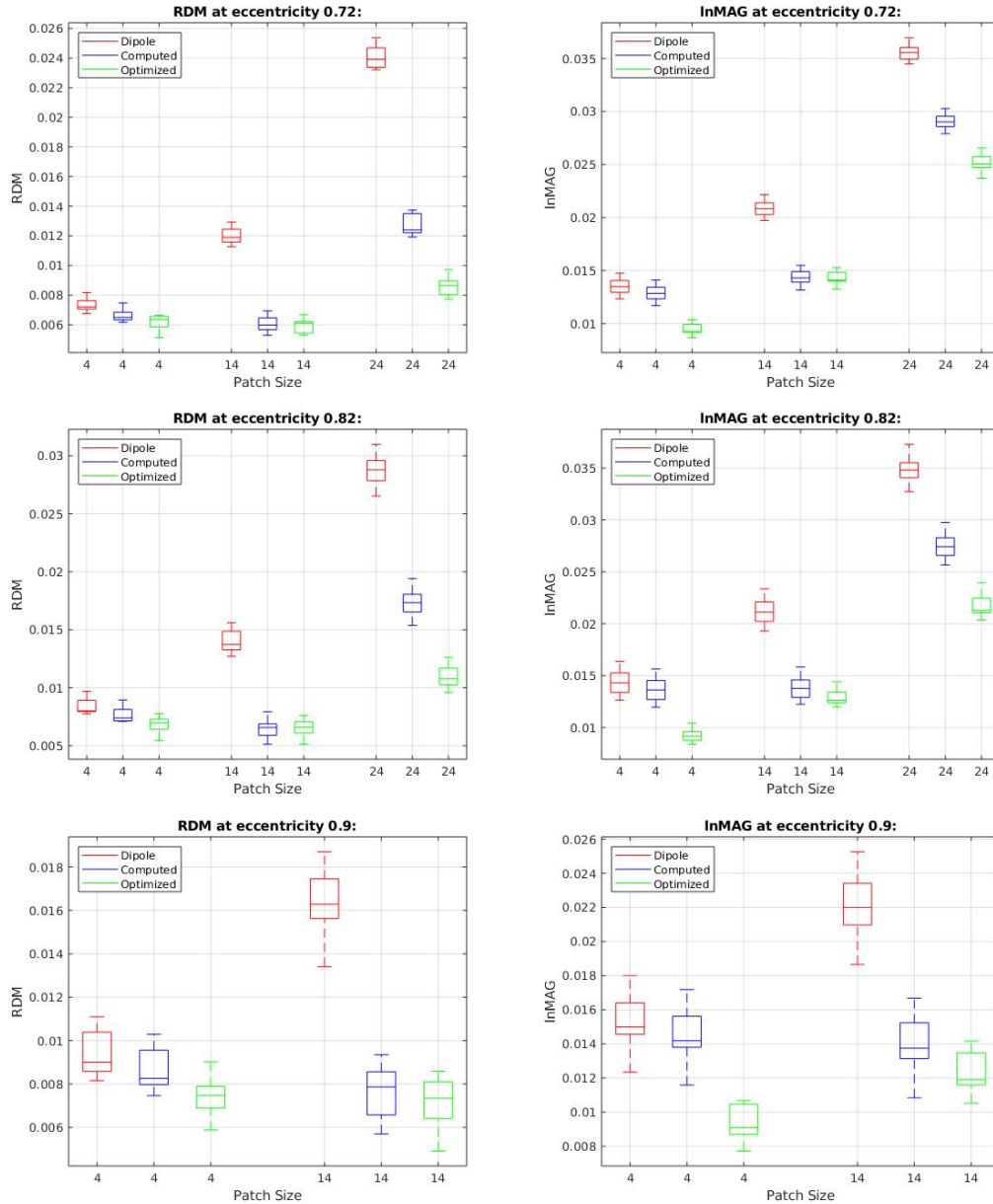


Figure 5.16: RDM (left column) and InMAG (right column) for radial patches at eccentricity 0.72 (top row), 0.82 (mid row) and 0.9 (bottom row) for model hex. Comparing the multipolar Venant approach using only dipolar moments (*Dipole*), multipolar moments with computed quadrupolar moments (*Computed*) and multipolar moments optimized quadrupolar moments (*Optimized*).

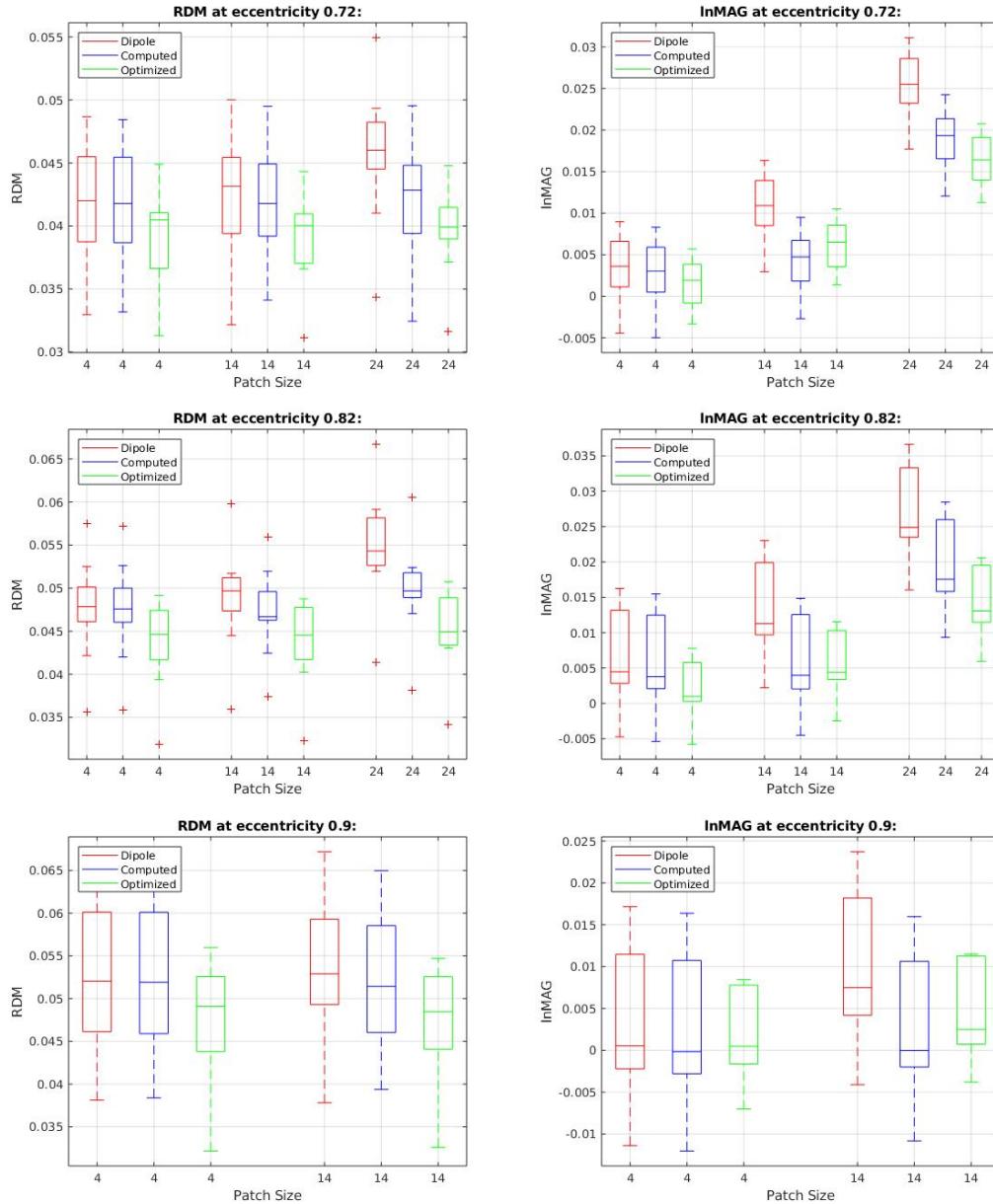


Figure 5.17: RDM (left column) and InMAG (right column) for radial patches at eccentricity 0.72 (top row), 0.82 (mid row) and 0.9 (bottom row) for model *tet\_low*. Comparing the multipolar Venant approach using only dipolar moments (*Dipole*), multipolar moments with computed quadrupolar moments (*Computed*) and multipolar moments optimized quadrupolar moments (*Optimized*).

Table 5.5: Optimized and computed quadrupolar moments. Dipole at position (63,0,0) with moment (1,0,0) as original dipole.

Mesh		Patch Size		
		4	14	24
tet_high	$m_{quad}[1, 1]$	-0.0105	-0.0772	-0.1864
	$m_{quad}[2, 2]$	0.0061	0.0736	0.1829
	$m_{quad}[3, 3]$	0.0138	0.0811	0.1903
	$m_{quad}[1, 2]$	0.0204	0.0223	0.0270
	$m_{quad}[2, 3]$	0.0234	0.0243	0.0264
	$m_{quad}[1, 3]$	0.0156	0.0137	0.0104
tet_low	$m_{quad}[1, 1]$	-0.1020	-0.1859	-0.2473
	$m_{quad}[2, 2]$	-0.2112	-0.1807	0.0052
	$m_{quad}[3, 3]$	0.1648	0.1838	0.2813
	$m_{quad}[1, 2]$	0.0450	0.0495	0.0593
	$m_{quad}[2, 3]$	-0.0310	-0.0317	-0.0311
	$m_{quad}[1, 3]$	0.0341	0.0274	0.0117
hex	$m_{quad}[1, 1]$	-0.1106	-0.1622	-0.2494
	$m_{quad}[2, 2]$	0.1295	0.1798	0.2634
	$m_{quad}[3, 3]$	0.0823	0.1396	0.2335
	$m_{quad}[1, 2]$	-0.0045	-0.0061	-0.0079
	$m_{quad}[2, 3]$	0.0084	0.0080	0.0070
	$m_{quad}[1, 3]$	-0.0172	-0.0161	-0.0138
computed	$m_{quad}[1, 1]$	0	0	0
	$m_{quad}[2, 2]$	0.0265	0.2778	0.7937
	$m_{quad}[3, 3]$	0.0265	0.2778	0.7937
	$m_{quad}[1, 2]$	2.7756e-17	2.7756e-17	1.3531e-16
	$m_{quad}[2, 3]$	4.3368e-19	-4.3368e-19	2.2768e-18
	$m_{quad}[1, 3]$	0	-8.6736e-19	0

As a second experiment, we want to take a closer look at radial dipoles and patches. We have seen that the use of quadrupolar moments clearly improves the approximation of extended sources in this scenario. Now we want to look at the exact values that result from the optimization and computation and therefore we will only consider one dipole at position (63,0,0) with moment (1,0,0) as original dipole. All parameters to build the patches remain the same as before, which means that we use the grid width  $h = 0.5$  mm and patch sizes  $n = 4, 14, 24$ . At first we determine the optimized quadrupole moments to this dipole for the different patch sizes and meshes. Also we compute the corresponding quadrupolar moments as defined in 4.6. See table 5.5 for the resulting values.

To begin with we observe that the diagonal values of the corresponding tensors,  $m_{quad}[i, i]$ , are bigger than the non-diagonal entries for nearly all scenarios. Moreover we see that the computed quadrupolar moments have the moment zero in direction of the dipolar moment and very small values at the non-diagonal entries. In contrast, the diagonal values for the directions orthogonal to the dipolar moment are bigger than for the optimized quadrupoles, at least for patch size 14 and 24. For patch size 4, the computed quadrupolar moments are rather small altogether. This fits to the finding that patches of this size are quite well represented by a pure dipole, anyway.

In order to get a better idea of the distribution of the different quadrupolar moments, we want to visualize them as ellipsoids. In order to visualize a tensor, we have to compute the eigenvalues and eigenvectors. See table 5.6 for the results.

We observe that the eigenvectors mainly have one main direction: In the first column they point almost in x direction, in the second column in y and in the third column in z direction. Nonetheless, they are not exactly pointing at the main axes of the coordinate system, so we computed the corresponding euler angles and rotated the ellipsoids with the resulting angles. See figures 5.18 - 5.21 for the results. Additionally to the ellipsoids representing the quadrupolar moments, there is also a blue line representing the direction of the dipole moment to be seen. For better visualization we cut the dipolar moments at 0.5, so the moment should be imagined as twice as long as it is in the plots.

In figure 5.18 you see the resulting visualized tensors for the tet\_high mesh for each patch size. For patch size 4 we see that the ellipsoid is rather small. As we have seen in figure 5.15, the difference between the dipole and multipole approach is also small, and thus this result also tells us that the small patch is already well represented by the pure dipole. Nevertheless, the biggest extend of the ellipsoid is in y direction, so it mainly represents the extent in this direction orthogonally to the dipole moment. For patch size 14 we see that the ellipsoid is already much bigger. Here we see that the extent in z direction with around 0.1 is similar to the extent in x direction, which is the direction of the dipole moment. The extent in y direction is a bit smaller and amounts to around 0.05. Thus we see that the quadrupolar moments here on the one hand represent the extend in z and y direction and therefore in the direction of the patch's extent, but on the other hand have some strength in (or against) the direction of the dipole moment. For patch size 24 we see that the ellipsoid again got bigger and more spherical. It shows similar trends and more strength in all directions, which results from the bigger extent of the patch. This also fits to the findings in figure 5.15, where the improvement of using the multipole instead of a pure dipole increases with increasing patch size.

For the results for the hex mesh see figure 5.19. For patch size 4, the ellipsoid has a similar shape as for the tet\_high mesh, but it is already profoundly bigger. This, and all other bigger values for the quadrupolar moments when looking at the hex mesh, could result from the fact that the solutions for the hex mesh generally show higher errors than for the tet\_high mesh. Therefore our optimization algorithm and the resulting quadrupolar moment might additionally compensate for the modeling errors of the mesh and therefore have a greater impact than for the tet\_high mesh. This also fits to the findings from figure 5.16, where we saw that the difference between the multipole and the pure dipole for the hex mesh is even more significant than for the tet\_high mesh. However, looking at the bigger patch sizes, again we see that the ellipsoids volumes are rising. For the hex mesh the shape, again, gets more spherical with increasing patch. This means that the quadrupolar moments show approximately the same strength in all directions.

For the tet\_low mesh in figure 5.20 we see that for patch size 4 the shape of the ellipsoid is different. It is more extended in z and y direction and less in x direction. This indicates that for this patch size the quadrupole moments represent the extent of the patch, but rarely the dipole moment's direction. Contrary to that, for patch size 14 and 24 the ellipsoids show a relatively strong extent in x direction, but a small one in y direction. So here the representation in (or against) the direction of the dipole moment has a greater impact. This again might result from the fact that the tet\_low mesh is rather coarse and therefore has high modeling errors, so we may get comparatively high values for the quadrupole moments in x direction as they compensate some modeling errors, too.

Table 5.6: Eigenvectors and -values to the quadrupolar moments.

Mesh	Patch Size	Eigen- value	vector	value	vector	value	vector
tet_high	4	-0.0242	-0.8276	0.0451	-0.4142	-0.0115	-0.3788
			0.5613		-0.6178		-0.5507
			-0.0059		-0.6684		0.7438
	14	-0.0811	0.9891	0.0532	0.0558	0.1054	0.1361
			-0.1326		0.7390		0.6605
			-0.0637		-0.6714		0.7384
	24	-0.1886	0.9972	0.1605	0.0377	0.2149	0.0641
			-0.0709		0.7420		0.6667
			-0.0224		-0.6694		0.7426
tet_low	4	-0.0876	0.9298	-0.2316	-0.3504	0.1708	-0.1128
			0.3590		0.9309		0.0672
			-0.0815		0.1030		-0.9913
	14	-0.2370	-0.7192	-0.1338	0.6920	0.1880	-0.0627
			0.6878		0.7218		0.0771
			0.0986		0.0123		-0.9950
	24	-0.2611	0.9747	0.0155	0.2233	0.2848	0.0098
			-0.2209		0.9692		-0.1085
			-0.0337		0.1036		0.9940
hex	4	-0.1122	0.9961	0.1312	-0.0311	0.0822	-0.0832
			0.0155		0.9832		-0.1819
			0.0874		0.1799		0.9798
	14	-0.1632	-0.9985	0.1816	-0.0266	0.1388	0.0484
			-0.0165		0.9800		0.1981
			-0.0527		0.1970		-0.9790
	24	-0.2499	-0.9995	0.2652	-0.0210	0.2322	0.0242
			-0.0150		0.9743		0.2249
			-0.0283		0.2244		-0.9741
computed	4	0	1	0.0265	0	0.0265	0
			0		1		0
			0		0		1
	14	0	1	0.2778	0	0.2778	0
			0		1		0
			0		0		1
	24	0	1	0.7937	0	0.7937	0
			0		1		0
			0		0		1

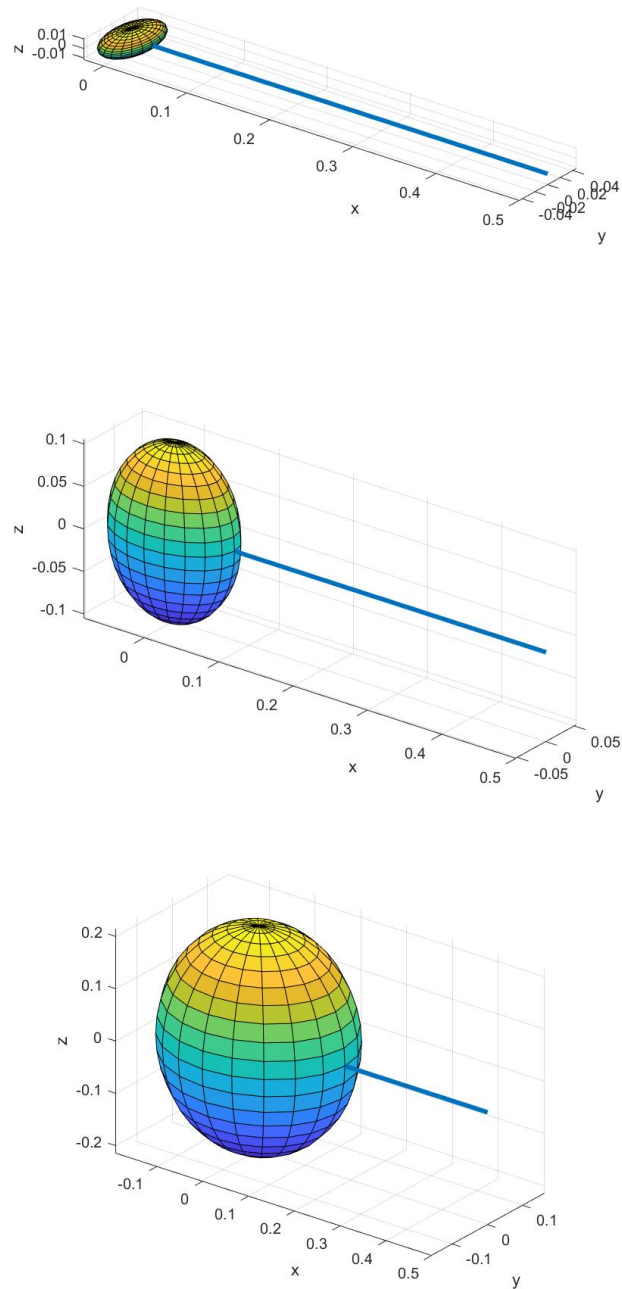


Figure 5.18: Ellipsoids for the tet\_high mesh. In the top row for patch size 4, mid row for patch size 14 and bottom row for patch size 24. See table 5.6 for the corresponding values. The blue line represents the direction of the dipolar moment.

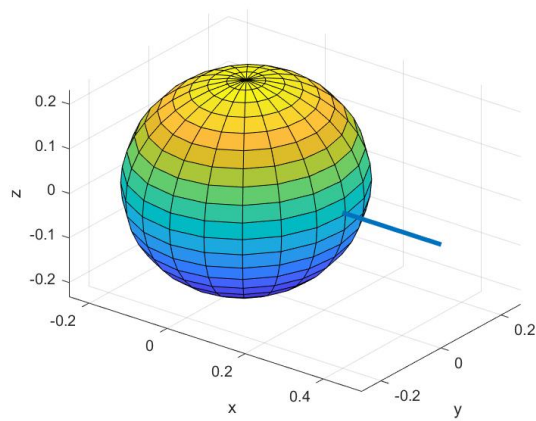
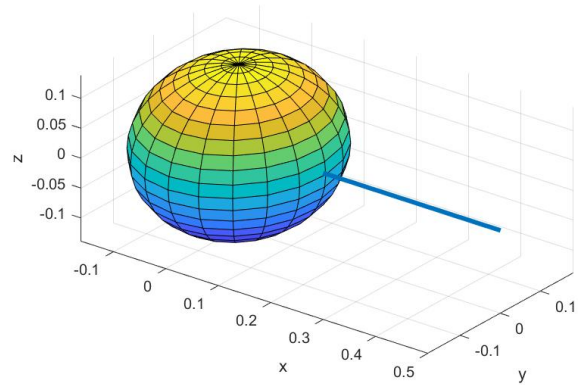
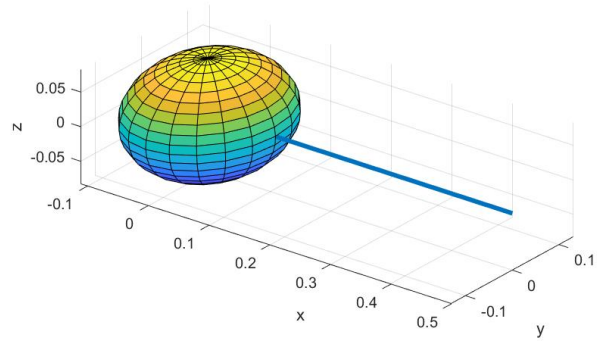


Figure 5.19: Ellipsoids for the hex mesh. In the top row for patch size 4, mid row for patch size 14 and bottom row for patch size 24. See table 5.6 for the corresponding values. The blue line represents the direction of the dipolar moment.

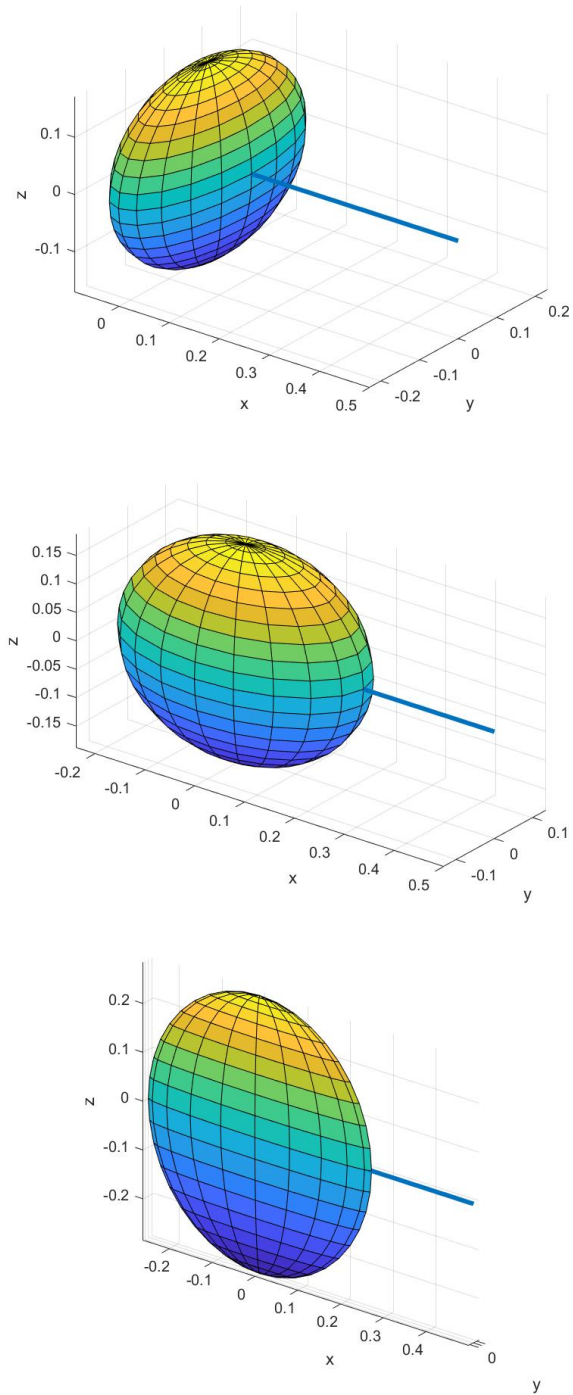


Figure 5.20: Ellipsoids for the tet\_low mesh. In the top row for patch size 4, mid row for patch size 14 and bottom row for patch size 24. See table 5.6 for the corresponding values. The blue line represents the direction of the dipolar moment.

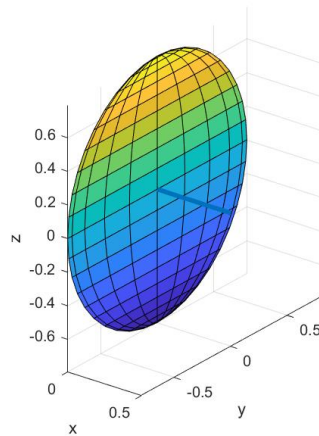
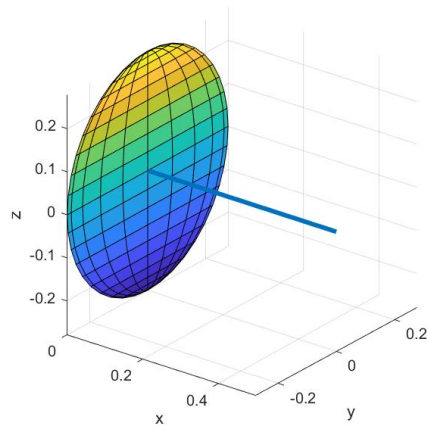
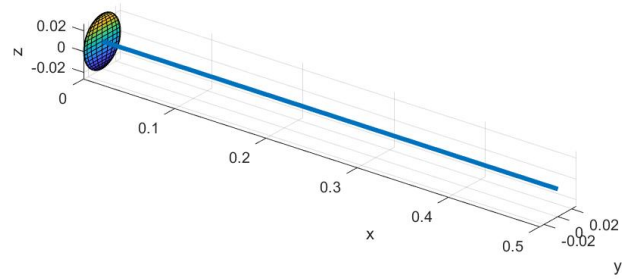


Figure 5.21: Ellipsoid for the computed quadrupolar moments. In the top row for patch size 4, mid row for patch size 14 and bottom row for patch size 24. See table 5.6 for the corresponding values. The blue line represents the direction of the dipolar moment.

In figure 5.21 one can see the visualization of the tensors for the computed quadrupolar values. As one can easily deduce from the values in table 5.6, they are in fact only two dimensional circles with a rising radius. We observe that the absence of extent in the direction of the dipole moment is the main difference between the computed and the optimized quadrupolar moments. Also, as already mentioned before, we see that for patch sizes 14 and 24 the extent in y and z direction is bigger than for all optimized quadrupolar moments.

All in all, the visualization of the quadrupolar moment tensors indicates that moments only in the directions orthogonal to the dipole moment, like the computed quadrupolar moments, can already improve the approximation of extended sources quite well. This shape is what one might expect, as these are the directions that cannot be represented by a pure dipole. On the contrary we have seen that all optimized quadrupolar moments also have extent in (or against) the direction of the dipole moment. There might be different reasons to that. On the one hand, it can simply arise from the fact that these moments compensate for modeling errors, which always occur when using a FEM mesh. On the other hand, they might represent the moments arising from the patch that point in the opposite direction of the dipole moment. One way or the other, the direction of the dipolar moment seems to be important when trying to find optimal quadrupolar moments and should therefore be considered when trying to find an optimized way to compute quadrupolar moments.

However, we have seen that the use of quadrupolar moments can strongly improve the approximation of extended sources. As expected, we got the best results when using optimized quadrupolar moments, but this is not applicable in realistic scenarios. For the determination of optimized quadrupolar moments we did not only need the knowledge about the patch's position and extent, but also an analytical solution as a goal function. In realistic head models, there is no analytical solution, which is why the optimization could not be applied. On top of that the computational effort of the optimization is too high to be applicable for a high number of sources even in a spherical head model.

Fortunately, we have also seen a way to compute the quadrupolar moments and, although it does not perform as well as the optimal quadrupoles, it still clearly improves the approximation of extended sources. In order to determine the computed quadrupoles, one needs to know the positions and moments of the patch dipoles. This could be applied in practice, too. One could try to create a patch, position it at different locations of a realistic head model and determine some positions within this patch as the positions of the patch dipoles. This patch generally would not be as regular as our patches, but adapted to the gyrus. The patch dipoles' moments should then be determined as being orthogonal to the gyrus. It could be an interesting future goal to test the computed quadrupolar moments in a realistic scenario. Moreover one could try to even improve the computation by adapting the equation so that it leads to quadrupoles shaped more similarly to the optimized ones, i.e. with some extent in (or against) the dipole moment's direction.

## 6 Conclusion

In this thesis we have seen different ways to solve the EEG forward problem using the principle of Saint Venant. We have modeled the source of brain activity as a monopole distribution instead of a mathematical dipole. This provided us with a way to use the Finite Element Method and avoid the singularity produced by a mathematical point dipole. Besides the well known monopolar Venant approach without mixed moments, we have looked at the monopolar Venant approach with mixed moments, which has been introduced by [NÜ18]. On top of that, we considered a relatively new approach using the Principle of Saint Venant, the multipolar Venant approach. This one has been introduced by [HA19] and [VO+19]. As part of the work for this thesis, the multipolar Venant approach has been implemented in the software DUNEuro, which has been used for all performed experiments.

In the numerical experiments, the multipolar Venant approach has been compared to the monopolar Venant approach with and without mixed moments. Using a 4-layer-sphere model with different meshes, the multipolar Venant approach has shown good results and outperformed the monopolar Venant approaches in many scenarios. The only lack of accuracy occurred when the use of the Venants Condition led to a too low number of monopole locations. Here the multipolar Venant approach seemed to be more sensitive than the monopolar Venant approaches. At any rate, this problem should be avoided in realistic scenarios as one should always ensure that the mesh is fine enough, in order for all neighboring vertices of a possible source to be within the brain compartement. Therefore, in realistic scenarios the multipolar Venant approach seems to outperform the monopolar approaches. To ensure this, more tests should be conducted, especially with realistic head models, but the findings of [HA19] and [VO+19] suggest that the multipolar Venant approach will show good performance in these scenarios, too.

As a last point, we investigated extended sources. The experiments have shown that the approximation can be strongly improved using multipoles instead of pure dipoles, at least for radial patches. We have seen two ways to determine the quadrupolar moments, an optimization and a computation. The optimized quadrupoles have shown the best overall performance, but the computed quadrupoles have shown a strong improvement in comparison to the pure dipole, too. On top of that, we have visualized the optimized and computed quadrupoles. This led us to the conclusion that the main difference between these two approaches is that the computed quadrupoles only have extent in the directions orthogonal to the dipole moment, while the optimized ones have extent in the dipole moments direction, too. This result might be used to find an even optimized way to compute quadrupolar moments. In order to make quadrupoles useable in realistic scenarios further investigations have to be done. The next step might be to test the computed quadrupoles in a realistic head model. In any case, this thesis has shown that the use of quadrupoles makes a strong difference and therefore further investment in this topic is worth the effort.

All in all, we saw that the multipolar Venant approach provides a good way to compute the EEG forward problem. Being used as a dipolar model, it shows a good performance in comparison to known approaches. Additionally, since it is based on multipole expansion, it provides a simple way to add quadrupole moments to the computation. In future research more tests should be conducted in realistic head models and also for MEG. The multipolar Venant approach might then turn out to be the best approach to use for combined EEG/MEG analysis and to represent extended sources.

## References

- [AC+10] Z.A. Acar, S. Makeig. *Neuroelectromagnetic forward head modeling toolbox*. Journal of neuroscience methods, 190(2):258-270, 2010.
- [BA+18] D. Baillot, University of California - San Diego. *Why are neuron axons long and spindly? Study shows they're optimizing signaling efficiency*. ScienceDaily, 11 July 2018. <[www.sciencedaily.com/releases/2018/07/180711153609.htm](http://www.sciencedaily.com/releases/2018/07/180711153609.htm)>.
- [BA+15] M. Bauer, S. Pursiainen, J. Vorwerk, H. Köstler, C.H. Wolters. *Comparison study for Whitney (Raviart-Thomas)-type source models in finite-element-method-based EEG forward modeling*. IEEE Transactions on Biomedical Engineering, 62(11):2648-2656, 2015.
- [BE18] L. Beltrachini. *A Finite Element Solution of the Forward Problem in EEG for Multipolar Sources*. IEEE Transactions on Neural Systems and Rehabilitation Engineering, Vol 27, No. 3, 2018.
- [BE19] L. Beltrachini. *Sensitivity of the projected subtraction approach to mesh degeneracies and its impact on the forward problem in EEG*. IEEE Transactions on Biomedical Engineering, 66(1):273-282, 2019.
- [BR13] D. Braess. *Finite Elemente: Theorie, schnelle Löser und Anwendungen in der Elastizitätstheorie*. 5. Auflage, Springer-Verlag Berlin Heidelberg, 2013.
- [BR+07] S. Brenner, R. Scott. *The mathematical theory of finite element methods*. Volume 15, Springer Science & Business Media, 2007.
- [BU+97] H. Buchner, G. Knoll, M. Fuchs, A. Rienäcker, R. Beckmann, M. Wagner, J. Silny, J. Pesh. *Inverse localization of electric dipole current sources in finite element models of the human head*. In: Electroencephalography and clinical Neurophysiology 102 (1997), pp. 267-278.
- [CO+06] M.J. Cook, Z.J. Koles. *A high-resolution anisotropic finite-volume head model for eeg source analysis*. Engineering in Medicine & Biology Society, 2006. EMBS'06. 28th Annual International Conference of the IEEE, pages 4536-4539. IEEE.
- [DM+88] J. de Munck, B. van Dijk, H. Spekkreijse. *Mathematical dipoles are adequate to describe realistic generators of human brain activity*. In: IEEE Trans. Biomed. Eng. 35(11) (1988), pp. 960-966.
- [DM+93] J. de Munck, M.Peters. *A fast method to compute the potential in the multi-sphere model*. IEEE Transactions on Biomedical Engineering 40 (11) (1993) 1166-1174, ISSN 0018-9294.
- [DR+09] F. Drechsler, C. Wolters, T. Dierkes, H. Si, L. Grasedyck. *A full subtraction approach for finite element method based source analysis using constrained Delaunay tetrahedralisation*. NeuroImage, 46(4):1055-1065, 2009.
- [GR+11] A. Gramfort, T. Papadopoulo, E. Olivi, M. Clerc. *Forward field computation with openmeeg*. Computational intelligence and neuroscience, 2011.
- [HÄ+93] M. Hämäläinen, R. Hari, R.J. Ilmoniemi, J. Knuutila, O.V. Lounasmaa. *Magnetoencephalography - theory, instrumentation, and applications to noninvasive studies of the working human brain*. Reviews of modern Physics, 65(2):413, 1993.
- [HA19] A. Hanrath. *Finite Element Representation of the EEG Forward Problem with Multipole Expansion*. Dissertation, RWTH Aachen University, 2019.

- [HÜ21] J. Hüwel *Effects of Source Modeling in the Finite Element Method Based EEG Forward Problem*. Masterthesis, Westfälische Wilhelms Universität Münster, 2021.
- [JA99] J. D. Jackson. *Classical Electrodynamics*. John Wiley & Sons, New York, NY, 3rd ed. edn., ISBN 978-0-471-30932-1, 1999.
- [JE+02] K. Jerbi, J.C. Mosher, S.Baillet, R.M. Leahy. *On MEG forward modeling using multipolar expansions*. *Physics in Medicine and Biology*, 47(4):523-55, 2002.
- [JE+04] K. Jerbi, J.C. Mosher, G. Nolte, L. Garnero, R.M. Leahy. *Localization of realistic cortical activity in MEG using current multipoles*. *NeuroImage* 22 (2004) 779-793.
- [KR19] J. Kramps: *Numerische Untersuchungen zu den Auswirkungen der Quellmodelle auf das FEM-basierte MEG-Vorwärtsproblem*. Masterthesis, 2019.
- [LE+09] S. Lew, C.H. Wolters, T. Dierkes, C. Röer, R.S. Macleod. *Accuracy and run-time comparison for different potential approaches and iterative solvers in finite element method based EEG source analysis*. *Applied Numerical Mathematics*, 59(8):1970-1988, 2009.
- [MA65] J.C. Maxwell. *A Dynamical Theory of the Electromagnetic Field*. *IPhil. Trans. R. Soc. Lond.* 155 (1865), pp. 459-512, 1865.
- [ME15] T. Medani, D. Lautru, Z. Ren, D. Schwartz, G. Sou. *FEM Method for the EEG Forward Problem and Improvement Based on Modification of the Saint Venant Method*. *Progress In Electromagnetics Research*, Vol. 153, 11-22, 2015.
- [MI+19] T. Miinalainen, A. Rezaei, D. Us, A. Nüßing, C. Engwer, C.H. Wolters, S. Pursiainen. *A realistic, accurate and fast source modeling approach for the EEG forward problem*. *NeuroImage*, 184:56-67, 2019.
- [MO+14] V. Montes-Restrepo, P. van Mierlo, G. Strobbe, S. Staelens, S. Vandenberghe, H. Hallez. *Influence of skull modeling approaches on eeg source localization*. *Brain topography*, 27(1):95-111, 2014.
- [MO+99] J.C. Mosher, R.M. Leahy, P.S. Lewis. *EEG and MEG: forward solutions for inverse methods*. *IEEE Transactions on Biomedical Engineering*, 46(3):245-259, 1999.
- [NÜ18] A. Nüßing. *Fitted and Unfitted Finite Element Methods for Solving the EEG Forward Problem*. Dissertation, Westfälische Wilhelms Universität, 2018.
- [NU+00] P.L. Nunez, R.B. Silberstein. *On the relationship of synaptic activity to macroscopic measurements: does co-registration of EEG with fMRI make sense?* *Brain Topogr.* 13, 79-96, 2000.
- [PU+11] S. Pursiainen, A. Sorrentino, C. Campi, M. Piana. *Forward simulation and inverse dipole localization with the lowest order Raviart-Thomas elements for electroencephalography*. *Inverse Problems*, 27(4):045003, 2011.
- [PU+16] S. Pursiainen, J. Vorwerk, C.H. Wolters. *Electroencephalography (EEG) forward modeling via  $H(\text{div})$  finite element sources with focal interpolation*. *Physics in Medicine & Biology*, 61(24): 8502, 2016.
- [SC+20] S. Schrader, A. Westhoff, M.C. Piastra, T. Miinalainen, S. Pursiainen, J. Vorwerk, H. Brinck, C.H. Wolters, C. Engwer. *DUNEuro - A software toolbox for forward modeling in bioelectromagnetism*. *PLoS ONE* 16(6): e0252431. <https://doi.org/10.1371/journal.pone.0252431>, 2021.
- [ST+12] M. Stenroos, J. Sarvas. *Bioelectromagnetic forward problem: isolated source approach revis(it)ed*. *Physics in Medicine & Biology*, 57(11):3517, 2012.

- [TA+05] I.O. Tanzer, S. Järvenpää, J. Nenonen, E. Somersalo. *Representation of bioelectric current sources using Whitney elements in the finite element method*. Physics in Medicine and Biology, 50(13):3023-3039, 2005.
- [VA+09] F. Vatta, F. Meneghini, F. Esposito, S. Mininell, F. Di Salle. *Solving the forward problem in eeg source analysis by spherical and fdm head modeling: a comparative analysis*. Biomedical sciences instrumentations, 45:382-288, 2009.
- [VO11] J. Vorwerk. *Comparison of Numerical Approaches to the EEG Forward Problem*. Diploma Thesis, Westfälische Wilhelms Universität Münster, 2011.
- [VO16] J. Vorwerk. *New Finite Element Methods to Solve the EEG/MEG Forward Problem*. Dissertation, Westfälische Wilhelms Universität Münster, 2016.
- [VO+18] J. Vorwerk, R. Oostenveld, M. C. Piastra, L. Magyari, C.H. Wolters. *The FieldTrip-SimBio pipeline for EEG forward solutions*. Biomedical engineering online 17 (1) (2018) 37, 2018.
- [VO+19] J. Vorwerk, A. Hanrath, C.H. Wolters, L. Grasedyck *The multipole approach for EEG forward modeling using the finite element method*, Neuroimage. 2019 Nov 1;201:116039. doi: 10.1016/j.neuroimage.2019.116039. Epub 2019 Jul 29. PMID: 31369809, 2019.
- [WE+00] D. Weinstein, L. Zhukov, C. Johnson. *Lead-field bases for electroencephalography source imaging*. Annals of biomedical engineering, 28(9):1059-1065, 2000.
- [WE+08] K. Wendel, N.G. Narra, M. Hannula, P. Kauppinen, J. Malmivuo. *The influence of csf on eeg sensitivity distributions of multilayered head models*. IEEE Transactions on Biomedical Engineering, 55(4):1454-1456, 2008.
- [WO+07a] C.H. Wolters, A. Anwander, G. Berti, U. Hartmann. *Geometry-Adapted Hexahedral Meshes Improve Accuracy of Finite-Element-Method-Based EEG Source Analysis*. IEEE Trans Biomed Eng. 2007a;54(8):1446-1453.
- [WO+07b] C.H. Wolters, H. Köstler, C. Möller, J. Härtlein, L. Grasedyck, W. Hackbusch. *Numerical mathematics of the subtraction method for the modeling of a current dipole in EEG source reconstruction using finite element head models*. SIAM J Sci Comput. 2007b;30(1):24-45.
- [YA+91] Y. Yan, P. Nunez, R. Hart. *Finite-element model of the human head: scalp potentials due to dipole sources*. Medical and Biological Engineering and Computing, 29(5):475-481, 1991.